# Brecciation at the grain scale within the lithologies of the Winchcombe Mighei-like carbonaceous chondrite

Luke DALY [1,2,3,*], Martin D. SUTTLE [4], Martin R. LEE [1], John BRIDGES[5], Leon HICKS[5,6],
Pierre-Etienne M. C. MARTIN[1], Cameron J. FLOYD [1], Laura E. JENKINS[1], Tobias SALGE [7],
Ashley J. KING [7], Natasha V. ALMEIDA [7], Diane JOHNSON[8], Patrick W. TRIMBY[9],
Haithem MANSOUR[9], Fabian B. WADSWORTH[10], Gavyn ROLLINSON[11], Matthew J. GENGE [12],
James DARLING[13], Paul A. J. BAGOT[1,3], Lee F. WHITE[4], Natasha R. STEPHEN [12,14,15],
Jennifer T. MITCHELL [14,16], Sammy GRIFFIN [1], Francesca M. WILLCOCKS[14],
Rhian JONES [17], Sandra PIAZOLO[18], Joshua F. EINSLE[1], Alice MACENTE[1,19,20],
Lydia J. HALLIS [1], Aine O'BRIEN[1], Paul F. SCHOFIELD[7], Sara S. RUSSELL [7],
Helena BATES [7], Caroline SMITH[7], Ian FRANCHI [4], Lucy V. FORMAN [21], Phil A. BLAND[21],
David WESTMORELAND[9], Iain ANDERSON[9], Richard TAYLOR[22], Mark MONTGOMERY[22],
Mark PARSONS[22], Jérémie VASSEUR[23], Matthias van GINNEKEN [24],
Penelope J. WOZNIAKIEWICZ[24], Mark J. BURCHELL [24], Daniel HALLATT[24,25],
Luke S. ALESBROOK[24], Vassilia SPATHIS[24], Richard WORDEN[26], Julie BEHNSEN[27],
Kate BLACK[27], and the UK Fireball Alliance

[1]School of Geographical and Earth Sciences, University of Glasgow, Glasgow, UK
[2]Australian Centre for Microscopy and Microanalysis, The University of Sydney, Sydney, New South Wales, Australia
[3]Department of Materials, University of Oxford, Oxford, UK
[4]School of Physical Sciences, The Open University, Milton Keynes, UK
[5]Space Park Leicester, School of Physics and Astronomy, University of Leicester, Leicester, UK
[6]School of Geology, Geography, Environment, University of Leicester, Leicester, UK
[7]Planetary Materials Group, Natural History Museum, London, UK
[8]School of Aerospace, Transport and Manufacturing, Cranfield University, Bedford, UK
[9]Oxford Instruments Nanoanalysis, High Wycombe, UK
[10]Earth Sciences, Durham University, Durham, UK
[11]Camborne School of Mines, University of Exeter, Penryn, UK
[12]Department of Earth Science and Engineering, Imperial College London, London, UK
[13]School of the Environment, Geography and Geoscience, University of Portsmouth, Portsmouth, UK
[14]Plymouth Electron Microscopy Centre, University of Plymouth, Plymouth, UK
[15]Geological Society of London, London, UK
[16]School of Earth & Environmental Science and Characterization Facility, University of Minnesota, Minneapolis, Minnesota, USA
[17]Department of Earth and Environmental Sciences, University of Manchester, Manchester, UK
[18]School of Earth and Environment, University of Leeds, Leeds, UK
[19]School of Civil Engineering, University of Leeds, Leeds, UK
[20]Department of Civil and Environmental Engineering, University of Strathclyde, Glasgow, UK
[21]Space Science and Technology Centre, School of Earth and Planetary Science, Curtin University, Bentley, Western Australia, Australia
[22]Carl Zeiss Microscopy, Cambridge, UK
[23]Earth and Environmental Sciences, Ludwig-Maximilians-Universität, Munich, Germany
[24]Centre for Astrophysics and Planetary Science, Department of Physics and Astronomy, University of Kent, Canterbury, UK
[25]CNRS, INRAE, Centrale Lille, UMR 8207—UMET Unité Materiaux et Transformations, University Lille, Lille, France
[26]Department of Earth, Ocean and Ecological Sciences, University of Liverpool, Liverpool, UK
[27]School of Engineering, University of Liverpool, Liverpool, UK

**\*Correspondence**

Luke Daly, School of Geographical and Earth Sciences, University of Glasgow, Glasgow G12 8QQ, UK.
Email: luke.daly@glasgow.ac.uk

**Abstract**–The Mighei-like carbonaceous (CM) chondrites have been altered to various extents by water–rock reactions on their parent asteroid(s). This aqueous processing has destroyed much of the primary mineralogy of these meteorites, and the degree of alteration is highly heterogeneous at both the macroscale and nanoscale. Many CM meteorites are also heavily brecciated juxtaposing clasts with different alteration histories. Here we present results from the fine-grained team consortium study of the Winchcombe meteorite, a recent CM chondrite fall that is a breccia and contains eight discrete lithologies that span a range of petrologic subtypes (CM2.0–2.6) that are suspended in a cataclastic matrix. Coordinated multitechnique, multiscale analyses of this breccia reveal substantial heterogeneity in the extent of alteration, even in highly aqueously processed lithologies. Some lithologies exhibit the full range and can comprise nearly unaltered coarse-grained primary components that are found directly alongside other coarse-grained components that have experienced complete pseudomorphic replacement by secondary minerals. The preservation of the complete alteration sequence and pseudomorph textures showing tochilinite–cronstedtite intergrowths are replacing carbonates suggest that CMs may be initially more carbonate rich than previously thought. This heterogeneity in aqueous alteration extent is likely due to a combination of microscale variability in permeability and water/rock ratio generating local microenvironments as has been established previously. Nevertheless, some of the disequilibrium mineral assemblages observed, such as hydrous minerals juxtaposed with surviving phases that are typically more fluid susceptible, can only be reconciled by multiple generations of alteration, disruption, and reaccretion of the CM parent body at the grain scale.

# INTRODUCTION

Mighei-like carbonaceous (CM) chondrites contain ~7–11 wt% structural $H_2O$ (Alexander et al., 2012; Jarosewich, 1990; Kerridge, 1985; Lee, Hallis, et al., 2023; Vacher et al., 2020), owing to having been extensively aqueously altered to produce a suite of secondary minerals, for example, phyllosilicates, carbonates, and magnetite (Bunch & Chang, 1980; Rubin et al., 2007; Suttle et al., 2021; Zolensky et al., 1997). Thus, the primary mineralogy and textures acquired from the accretion of their parent body(ies) have been largely overprinted. Additionally, the majority of CM meteorites are breccias and experienced extensive disaggregation and reaccretion on the regolith of asteroids (Bischoff et al., 2017; Lee, Floyd, et al., 2023; Lentfort et al., 2021; Lindgren et al., 2013; Suttle et al., 2022; Verdier-Paoletti et al., 2019).

Aqueous alteration likely occurred in an asteroidal environment (Brearley, 2003, 2006; Rubin et al., 2007; Suttle et al., 2021) as evidenced by millimeter-scale reaction fronts and mineral veins (Chizmadia & Brearley, 2004; Hanowski & Brearley, 2000; Jacquet et al., 2016; Lee et al., 2012; Lindgren et al., 2017). This parent body alteration model is also supported by the observations of the water-

and organic-rich asteroid Bennu by the OSIRIS-REx spacecraft that has revealed centimeter-sized carbonate veins in boulders at its surface (Kaplan et al., 2020). However, recent analyses of the reflectance spectra of asteroid Bennu suggest it is more closely linked to CR chondrites than CMs (Hamilton et al., 2022).

Despite this pervasive aqueous alteration, CM chondrites preserve a primitive chemistry, in particular for water-soluble elements, for example, Ca, Na, and S (Brearley, 2003; Chizmadia & Brearley, 2004). This apparent contradiction can be reconciled if aqueous alteration was isochemical and occurred in a closed system environment (DuFresne & Anders, 1962; Kerridge et al., 1979; McSween Jr, 1979a) that precluded soluble element loss from CM lithologies. Potential mechanisms to limit the loss of volatile elements are localized alteration from accreted ices in a high-nano-porosity but low-permeability environment that limits fluid flow to <100 μm length scales over the duration of aqueous alteration (Bland et al., 2009), or convection of an unlithified "mud slurry" (Bland & Travis, 2017).

Studies of the least aqueously altered CM chondrites show that prior to aqueous alteration, the primary matrix of CM meteorites likely consisted of amorphous silicates, metal, carbide and sulfide grains, organics, presolar grains and minor anhydrous silicate minerals (e.g., forsterite and

enstatite) (Bland et al., 2007; Chizmadia & Brearley, 2008; Davidson et al., 2019; Kimura et al., 2020; Lee et al., 2019; Leroux et al., 2015; Noguchi et al., 2021; Rubin, 2015; Schmitt-Kopplin et al., 2010; Suttle et al., 2021). The amorphous phases are similar in morphology and texture to primitive glass with embedded metal and sulfide (GEMS) grains (Leroux et al., 2015) that are found in cometary dust (Bradley, 1994a; Noguchi et al., 2017). Where they occur in chondritic matrices, these phases have been referred to as "GEMS-like" (Leroux et al., 2015). However, other studies have suggested that there is no convincing evidence of GEMS in CM matrix (Ohtaki et al., 2021; Villalon et al., 2021). In addition, the matrix of CM chondrites would have likely accreted a substantial component of carbon-rich water ice (water/rock ratios of 0.2–0.7; Brearley, 2006; Clayton & Mayeda, 1999; Howard et al., 2015; Marrocchi et al., 2018; Suttle et al., 2020; Suttle et al., 2021; Zolensky et al., 1997), particles of which may have been relatively coarse grained (10–60 μm, based on the size of macropores and carbonate assemblages that grew into the pore space left behind when the ice melted) (Kimura et al., 2020; Lee et al., 2014; Matsumoto et al., 2019; Rubin et al., 2007).

These primary materials would have been highly susceptible to alteration by aqueous fluids (Chizmadia & Brearley, 2008; Davidson et al., 2014; Leroux et al., 2015; Nakamura-Messenger et al., 2011; Rubin, 2015; Rubin et al., 2007). Meteorite matrix has been proposed as a sensitive indicator for the extent of thermal and aqueous alteration as its porosity and fine grain size could allow fluids to permeate and access grain boundaries (McSween Jr, 1987; Rubin et al., 2007; Tomeoka et al., 1989). In addition, pore collapse during impact compaction could produce temperature spikes in the matrix to locally melt ices (Bland et al., 2014). An over-arching effect of progressive aqueous alteration of CM matrix is that the concentration of Mg increases as it is released from the alteration of chondrule olivine (Tomeoka et al., 1989).

Many of the original constituents of CM chondrites are modified during aqueous alteration (Brearley, 2006; Rubin et al., 2007; Suttle et al., 2021). The fine-grained matrix and coarser, more fluid-susceptible phases alter first and more fluid-resistant coarser components such as Mg silicates remain unaltered until high degrees of aqueous alteration (Brearley, 2006; Rubin et al., 2007; Suttle et al., 2021), that is, at petrologic subtypes, CM 2.0 on the Rubin et al. (2007) scale, where all primary components are completely altered (Brearley, 2006; Rubin et al., 2007; Suttle et al., 2021). However, even in these highly aqueously altered CM 2.0 meteorites, a small proportion of the primary mineralogy is preserved, for example, residual amorphous and anhydrous silicates (Hewins et al., 2014; Marrocchi et al., 2014; Rubin, 2015; Rubin et al., 2007; Suttle et al., 2021; Velbel et al., 2015). In less

aqueously altered CMs, unaltered regions that are micrometer to millimeter scale have been described within the matrix (Hewins et al., 2014; Kimura et al., 2020; Leroux et al., 2015) and disequilibrium assemblages where unaltered phases are in close proximity to, or even touching completely altered mineral phases in the matrix, tochilinite–cronstedtite intergrowths (TCIs) (Pignatelli et al., 2017) and fine-grained rims (FGRs) (Leroux et al., 2015; Metzler et al., 1992; Pinto et al., 2022).

Reconciling highly localized millimeter-nanoscale disequilibrium assemblages with parent body aqueous alteration could be explained by: (1) alteration behavior being locally controlled by heterogeneous grain size, mineralogy, and the differential solubility of minerals (Hanowski & Brearley, 2001; Zolensky et al., 1993); (2) varying the initial water/rock ratio of the asteroids and heterogeneous accretion of ices, where certain volumes contain more or less initial ice (Rubin et al., 2007) which would result in the localized survival of otherwise fluid sensitive phases as the reactive fluid is exhausted/consumed (Howard et al., 2015; Velbel et al., 2012); (3) limited permeability resulting in localized regions that experienced less alteration by fluids than others (Bland et al., 2009); (4) many CMs have a pervasive fabric defined by both chondrules and matrix (Hanna et al., 2015; Lindgren et al., 2015), which promotes heterogeneous alteration through anisotropic permeability (Zhang, 2013); (5) some or all of the secondary mineral assemblages may have been inherited from a precursor body or from the solar nebula (Metzler et al., 1992); (6) CM meteorites are breccias resulting in mixing and juxtaposition of materials with different aqueous alteration histories next to each other via regolith gardening (Bischoff et al., 2017; Brearley, 1995).

The Winchcombe meteorite is a CM chondrite that fell on February 28, 2021. The rapid recovery of the majority of the main mass within 12 h (Russell et al., 2022) means that it has experienced minimal terrestrial alteration (Jenkins et al., 2022; King et al., 2022). The Winchcombe meteorite is a complex breccia with eight petrographically distinct lithologies (A-H) identified so far, held within a cataclastic matrix (Mx) (King et al., 2022; Suttle et al., 2022). The degree of aqueous alteration of these lithologies ranges widely, giving petrologic subtypes of CM 2.0–2.6 (Suttle et al., 2022) on the scale of Rubin et al. (2007); Rubin (2015). Thus, the Winchcombe meteorite represents an ideal sample to assess the extent to which CMs have been aqueously altered and how that compares to overall petrologic subtype. Here we present a multi-length-scale coordinated study of the Winchcombe meteorite's texture, mineralogy, and extent of aqueous alteration of its fine-grained matrix (including carbonates, and TCIs) and

FGRs around chondrules, refractory inclusions, isolated mineral grains, and TCIs. The results are used to assess the nanoscale heterogeneity of aqueous alteration across a range of CM petrologic subtypes and to explore how disequilibrium mineral assemblages may arise in CM meteorites.

## METHODS

We applied a series of coordinated microanalytical methods to the Winchcombe meteorite. Each technique and the data acquired is briefly described below. Full methods including sample preparation, analytical instrumentation, analytical conditions, standards used, and how the data were processed are provided in File S1.

Twenty-two fragments (Table S1) of the Winchcombe meteorite were imaged using x-ray micro-computed tomography (μCT). Chondrule petrofabric and porosity measurements of all data sets were conducted using the Avizo© software. Porosity data were used to model the macroscale permeability of the meteorite.

Sixteen polished sections of the Winchcombe meteorite were analyzed by scanning electron microscopy with energy dispersive x-ray spectrometry (SEM-EDS) (Table 1) using a variety of SEM instrumentation. The data collected include secondary electron (SE), backscattered electron (BSE) images, energy dispersive x-ray spectrometry (EDS) maps, and point measurements, as well as EBSD maps. The EDS maps presented in this manuscript have not been background corrected. Quantitative EDS spot analyses were acquired from TCIs, matrix and FGRs, and secondary minerals associated with chondrules and calcium-aluminum-rich inclusions (CAIs) using a focused electron beam with a beam diameter <1 μm. 2-D chondrule and CAI shapes were extracted to determine the presence of any 2-D petrofabrics. Quantitative major and minor element data for Na, Mg, Al, Si, P, S, Cl, K, Ca, Ti, V, Cr, Mn, Fe, Co, and Ni were acquired from areas of matrix, FGRs and the interior and exterior of TCI clumps and chondrule phyllosilicates by wavelength-dispersive spectrometry (WDS) using an electron probe microanalysis (EPMA) instrument. The Winchcombe sections studied are the same as those described in Suttle et al. (2022) and comprise all of the Winchcombe lithologies A–H and the cataclastic matrix (Mx) and cover the range of petrologic types 2.0–2.6 (Table 1).

EDS and WDS-EPMA quantified spectra were assigned their section number, a Winchcombe lithology label based on Suttle et al. (2022), and a phase that reflects the type of material measured (matrix, FGR, TCI-core, TCI-rim, chondrule phyllosilicate, CAI phyllosilicate, etc.). Both wt% and atom% data for major and minor elements were calculated as well as wt% oxide ratios for $FeO/SiO_2$, and $S/SiO_2$ and atom% values for the Mg# and Si/Al,

$(Si+Al)/(Si+Al+Mg+Fe)$, $Mg/(Si+Al+Mg+Fe)$, $Fe/Si$, and $S/Si$ ratios as these are typical metrics for the alteration extent of CM meteorites (Supplementary Spreadsheets S1–S5).

Electron backscatter diffraction (EBSD) maps were acquired across partially altered chondrules, TCIs, carbonates, and the fusion crust within section P30555 (lithology A).

Focused ion beam time-of-flight secondary ion mass spectrometry (FIB-TOF-SIMS) data for negative and positive ions were collected from TCIs, FGRs, and the matrix of Winchcombe section P30550 (lithology A). Samples were extracted and prepared for transmission electron microscopy (TEM) and atom probe tomography (APT) using Ga and plasma-FIBs following established methods (Daly et al., 2021; Hicks et al., 2014; Lee et al., 2003). High-resolution TEM imaging, scanning-(S)TEM-EDS, and APT were performed to explore the nanoscale texture, mineralogy, and composition of fine-grained components such as phyllosilicates in Winchcombe.

## RESULTS

### Field Observations

The main mass of the Winchcombe meteorite recovered from a driveway in the town of Winchcombe, United Kingdom, shattered into thousands of fragments on impact with the surface (King et al., 2022). The recovery and curation of the Winchcombe meteorite along with descriptions of the various stones are described in Russell et al. (2022). Additional information relevant to the present study is that during collection of the fine fragments from the driveway over subsequent days by several individuals it was noted that many fragments exhibited flat sides and preferentially fractured along a "cleavage" plane.

### Winchcombe Lithologies

The Winchcombe meteorite contains eight lithologies (A–H) that form clasts suspended in a cataclastic matrix (Mx) (Suttle et al., 2022). The cataclastic matrix (Mx) is a fragmented mixture of all lithologies (Suttle et al., 2022). Letters were assigned to each lithology based on their exposed surface area, with A being the most abundant (26.3%) and H being the least abundant (0.2%) (Suttle et al., 2022). Three lithologies dominate (A–C) and cover >70% of the total area studied (Suttle et al., 2022). Lithologies were distinguished primarily from the abundance, composition, occurrence, and textural properties of TCIs, matrix, carbonates, metal and/or magnetite, and Fe-sulfides. Lithologies were also separated by clear boundaries (Suttle et al., 2022). Detailed accounts of the petrology and mineralogy of each of the lithologies

TABLE 1. Average chemical compositions, in atom% or atom% ratios, of the matrix, FGR, TCI-like object-rims, TCI-like object-cores, and phyllosilicates within chondrules, CAIs, and other clasts within the Winchcombe meteorite.

| Lithology | Subtype | Sample | Petrofabric | Matrix Mg# Mean | Matrix Mg# SD | Matrix Si/Al atom% Mean | Matrix Si/Al atom% SD | Matrix S atom% Mean | Matrix S atom% SD | FGR Mg# Mean | FGR Mg# SD | FGR Si/Al atom% Mean | FGR Si/Al atom% SD | FGR S atom% Mean | FGR S atom% SD | TCI rim Mg# Mean | TCI rim Mg# SD | TCI rim Si/Al atom% Mean | TCI rim Si/Al atom% SD | TCI rim S atom% Mean | TCI rim S atom% SD | TCI core Mg# Mean | TCI core Mg# SD | TCI core Si/Al atom% Mean | TCI core Si/Al atom% SD | TCI core S atom% Mean | TCI core S atom% SD | Phyllo Mg# Mean | Phyllo Mg# SD | Phyllo Si/Al atom% Mean | Phyllo Si/Al atom% SD | Phyllo S atom% Mean | Phyllo S atom% SD |
|---|---|---|---|---|---|---|---|---|---|---|---|---|---|---|---|---|---|---|---|---|---|---|---|---|---|---|---|---|---|---|---|---|---|
| A | 2.2 | P30550 | NM | 61.78 | 4.43 | 11.95 | 1.34 | 2.47 | 0.56 | ND | ND | ND | ND | ND | ND | 35.51 | 5.19 | 0.95 | 0.02 | 7.79 | 2.32 | 69.19 | 9.58 | 13.29 | 1.25 | 1.16 | 0.60 | 77.27 | 1.05 | 16.45 | 1.06 | 1.24 | 0.26 |
| | | P30551 | NM | ND | ND | ND | ND | ND | ND | ND | ND | ND | ND | ND | ND | 37.47 | 4.92 | 0.96 | 0.01 | 7.48 | 1.15 | 75.19 | 2.45 | 15.63 | 1.54 | 1.49 | 0.83 | ND | ND | ND | ND | ND | ND |
| | | P30552 | Moderate | 61.93 | 7.08 | 11.43 | 2.62 | 3.02 | 0.97 | 62.71 | 3.24 | 11.47 | 1.62 | 2.61 | 0.97 | 41.68 | 12.21 | 0.97 | 0.02 | 6.84 | 3.24 | 75.59 | 2.82 | 16.05 | 1.03 | 1.45 | 0.67 | ND | ND | ND | ND | ND | ND |
| B | 2.1 | P30424 | Random | 67.12 | 5.50 | 15.25 | 4.28 | 2.34 | 0.57 | ND | ND | ND | ND | ND | ND | 47.94 | 5.16 | 0.95 | 0.02 | 4.29 | 1.21 | 77.90 | 1.20 | 16.10 | 0.51 | 1.24 | 0.41 | 57.45 | 13.95 | 9.21 | 6.72 | 1.37 | 1.40 |
| | | P30542 | Moderate | 49.34 | 7.74 | 10.81 | 3.59 | 1.75 | 1.24 | 70.54 | 4.35 | 20.14 | 4.81 | 1.22 | 1.24 | 49.03 | 5.16 | 0.96 | 0.01 | 4.35 | 1.03 | 78.85 | 3.33 | 12.80 | 0.26 | 0.80 | 0.49 | ND | ND | ND | ND | ND | ND |
| | | P30544 | NM | 47.28 | 2.72 | 9.79 | 1.24 | 3.16 | 0.50 | ND | ND | ND | ND | ND | ND | 38.14 | 6.08 | 0.95 | 0.01 | 2.64 | 1.23 | 61.16 | 13.96 | 14.56 | 2.06 | 2.51 | 1.43 | ND | ND | ND | ND | ND | ND |
| | | P30545 | Weak | ND | ND | ND | ND | ND | ND | ND | ND | ND | ND | ND | ND | ND | ND | ND | ND | ND | ND | ND | ND | ND | ND | ND | ND | ND | ND | ND | ND | ND | ND |
| C | 2.2/2.3 | P30423 | Moderate | 62.83 | 4.88 | 11.00 | 1.48 | 2.68 | 0.53 | ND | ND | ND | ND | ND | ND | 15.92 | 5.02 | 0.98 | 0.03 | 4.02 | 2.14 | ND | ND | ND | ND | ND | ND | 54.36 | 31.12 | 10.83 | 1.66 | 0.46 | 0.29 |
| D | 2.6 | P30541 | Weak | 59.43 | 7.01 | 10.63 | 2.21 | 2.69 | 0.71 | 64.35 | 3.47 | 11.43 | 1.26 | 3.04 | 0.71 | 49.70 | 9.51 | 3.09 | 3.81 | 2.02 | 1.10 | 74.11 | 3.36 | 15.15 | 0.94 | 1.98 | 0.73 | 68.47 | 9.37 | 9.83 | 2.86 | 1.31 | 0.85 |
| E | 2.3 | P30541 | NM | 56.78 | 9.70 | 10.83 | 2.37 | 2.27 | 0.86 | 63.58 | 3.55 | 12.73 | 2.31 | 2.70 | 0.86 | 42.72 | 7.67 | 8.63 | 3.41 | 4.48 | 1.62 | ND | ND | ND | ND | ND | ND | 68.55 | 4.67 | 12.37 | 4.23 | 2.11 | 1.46 |
| | | P30548 | Strong | 58.66 | 3.08 | 12.26 | 1.39 | 1.94 | 0.55 | 57.67 | 7.43 | 10.76 | 1.21 | 1.70 | 0.55 | 33.63 | 8.42 | 0.95 | 0.01 | 4.98 | 1.94 | 60.51 | 6.24 | 11.98 | 1.18 | 4.36 | 0.83 | 17.56 | 2.70 | 5.23 | 1.18 | 0.31 | 0.43 |
| F | 2.0 | P30540 | Weak | 55.13 | 8.73 | 9.50 | 1.62 | 2.41 | 1.58 | ND | ND | ND | ND | ND | ND | 46.97 | 3.04 | 0.86 | 0.10 | 1.09 | 0.48 | 74.12 | 3.64 | 16.42 | 1.73 | 0.73 | 1.49 | ND | ND | ND | ND | ND | ND |
| G | 2.1 | P30540 | Weak | 65.06 | 7.11 | 11.47 | 1.37 | 2.06 | 0.60 | ND | ND | ND | ND | ND | ND | 36.68 | 4.50 | 0.92 | 0.03 | 1.78 | 0.58 | 73.46 | 8.22 | 14.11 | 0.44 | 2.92 | 0.53 | ND | ND | ND | ND | ND | ND |
| H | 2.3/2.4 | P30544 | NM | 55.91 | 5.93 | 22.32 | 2.87 | 3.62 | 0.42 | ND | ND | ND | ND | ND | ND | 22.26 | 4.13 | 0.95 | 0.01 | 7.16 | 5.80 | ND | ND | ND | ND | ND | ND | 40.47 | 0.45 | 4.31 | 0.73 | 0.11 | 0.05 |
| | | P30424 | NM | 62.64 | 7.88 | 12.82 | 3.47 | 2.43 | 0.76 | ND | ND | ND | ND | ND | ND | ND | ND | ND | ND | ND | ND | ND | ND | ND | ND | ND | ND | 67.77 | 10.34 | 11.81 | 4.88 | 1.11 | 0.58 |
| Mx | – | P30540 | Random | 59.95 | 5.70 | 10.68 | 2.08 | 2.33 | 0.76 | ND | ND | ND | ND | ND | ND | 30.34 | 6.61 | 0.95 | 0.02 | 2.97 | 2.55 | 76.59 | 0.68 | 16.90 | 0.45 | 1.05 | 0.16 | ND | ND | ND | ND | ND | ND |
| | | P30541 | NM | 61.94 | 4.68 | 13.26 | 2.56 | 2.02 | 0.42 | ND | ND | ND | ND | ND | ND | 34.10 | 7.95 | 0.95 | 0.03 | 4.82 | 3.01 | ND | ND | ND | ND | ND | ND | 68.54 | 4.66 | 12.41 | 4.26 | 2.11 | 1.46 |
| | | P30544 | NM | 54.85 | 7.45 | 11.32 | 2.36 | 3.10 | 1.54 | ND | ND | ND | ND | ND | ND | 11.11 | 10.49 | 0.93 | 0.03 | 2.70 | 1.16 | 73.33 | 1.16 | 15.31 | 1.74 | ND | ND | 27.93 | 23.09 | 14.95 | 8.95 | 0.73 | 1.04 |
| | | P30547 | NM | 57.77 | 9.23 | 10.79 | 2.22 | 2.86 | 1.07 | ND | ND | ND | ND | ND | ND | 30.70 | 9.07 | 0.93 | 0.03 | 2.76 | 2.44 | 71.16 | 2.44 | 13.30 | 0.50 | 3.03 | 0.33 | ND | ND | ND | ND | ND | ND |

Note: The presence or the absence of chondrule shape petrofabrics is also summarized. Data are subdivided by both lithology and section number. Abbreviations: ND, not detected; NM, not measured.

(A-H+Mx) in Winchcombe are presented in Suttle et al. (2022), so will not be repeated here. In addition, several seminal papers provide detailed descriptions of the fine-grained mineralogy of CM chondrites (Barber, 1981; Bunch & Chang, 1980; Chizmadia & Brearley, 2008; Fuchs et al., 1973; Leroux et al., 2015; Mackinnon, 1980; McSween Jr, 1979a, 1979b; Metzler et al., 1992; Rubin et al., 2007; Suttle et al., 2021; Tomeoka & Buseck, 1988; Velbel et al., 2012, 2015; Zanetta et al., 2021; Zolensky et al., 1993, 1997). As such, only additional data and observations that provide specific evidence for heterogeneities in the extent of aqueous alteration and textures that can be used to infer the primary mineralogy within each lithology, as well as descriptions of the matrix TCI and FGRs, will be presented in the main text. Detailed descriptions of the fine-grained mineral assemblages and textures for each lithology alongside other supporting observations can be found in the supplementary materials (Figures S1–S3).

## 3-D Petrofabrics

Of the 19 fragments of the Winchcombe meteorite where chondrule orientations were investigated by μCT, nine exhibit a random texture, and 10 show a foliation fabric (Figure 1a–c, Table S1, File S2) and one contains a fracture cleavage with a high density of subparallel fractures with a consistent trend that define lithological boundaries (Figure 1d). Three fragments with a foliation fabric also contained multiple lithologies (Figure 1c). In some cases, stereographic projections of chondrule orientations within juxtaposed lithologies show that the foliation planes defined by chondrule long axes in each sample are not parallel (90° apart), while in other cases they are subparallel (Figure 1c, Table S1, File S2). Additional descriptions of these textures are in File S1.

## 2-D Petrofabrics

Of the eight thick sections representing the eight lithologies A, B, C, D, E, F, G, and Mx, as defined by Suttle et al. (2022), that were investigated for 2-D chondrule petrofabrics, seven exhibited a weak-moderate preferred alignment of the long shape axes of chondrules or chondrule pseudomorphs (Figure 2, Table 1). Weak-moderate 2-D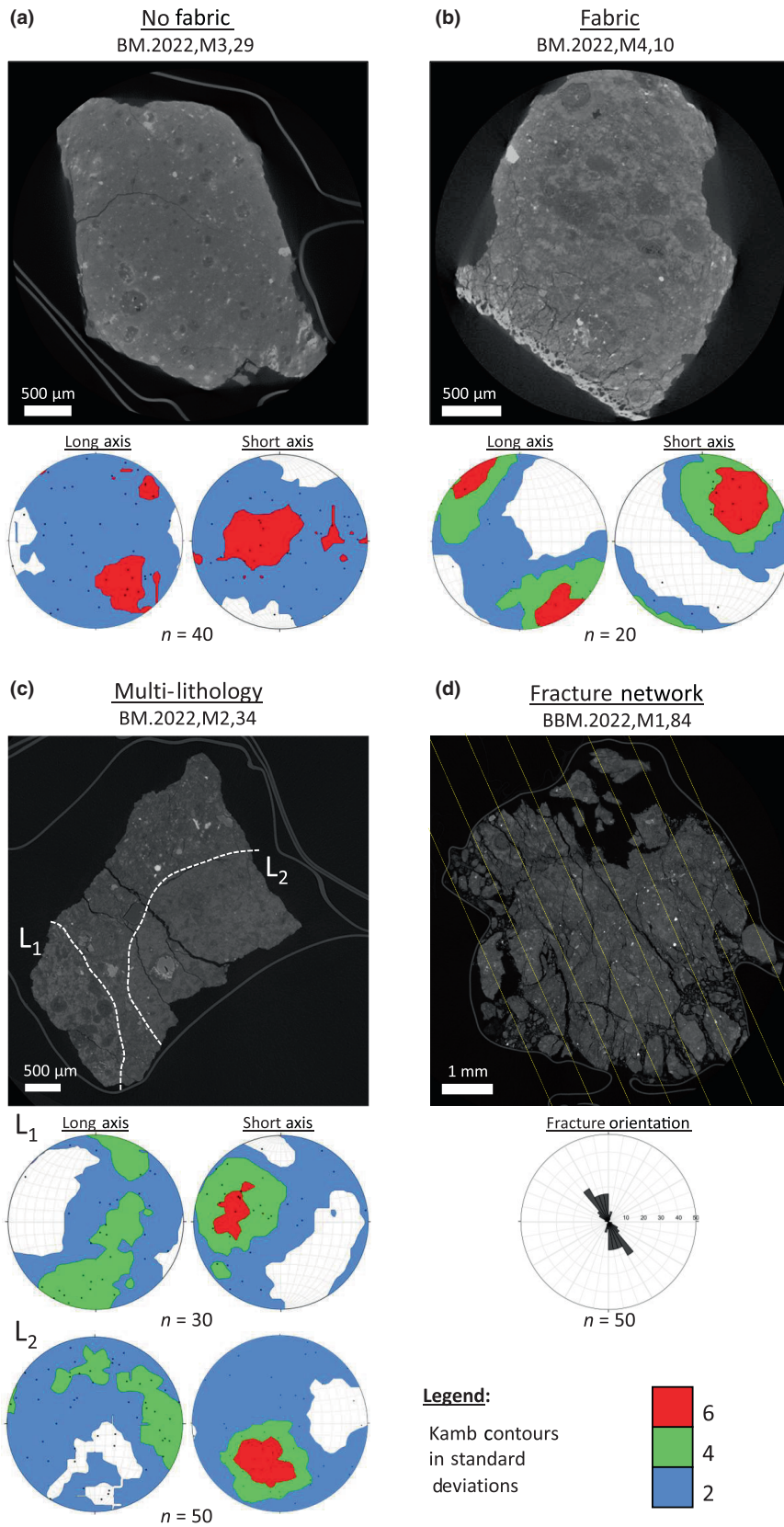 chondrule petrofabrics have been observed in lithologies A, B, C, D, E, F and G, and random textures have been observed in some parts of lithology B and in lithology Mx (Figure 2, Table 1). It should be noted, however, that the rarity of chondrules in lithology Mx (Figure 2h) mean that this is likely not an accurate measure of the lithology's texture. Lithology B in sections P30542 and P30545 shows one major moderate strength chondrule alignment, and possibly a second weak chondrule alignment that is perpendicular to the first (Figure 2b,c). In section P30542, the primary chondrule alignment was subparallel to the fusion crust (Figure 2b). The random texture observed in the lithology B in P30424 is likely to be a cutting artifact where the cut of the section was subparallel to the chondrule shape alignment as a moderate petrofabric was observed in other sections that contained lithology B (Figure 2b,d). At the micrometer scale, in the matrix of lithology B, coarse phyllosilicate laths (5–10 μm) appear to have a preferred alignment. Lithology B is also highly porous and a preferred alignment of the long shape axis of pores is observed. These pores are aligned perpendicular to the 2-D chondrule-defined fabric. The strongest 2-D chondrule petrofabrics were observed in lithology E (Figure 2g). The preferred alignments of chondrules in lithologies F and G are approximately perpendicular to each other (Figure 2h). Where petrofabrics have been observed in a 2-D section, the orientation of any macroscale fractures within these sections appears to run subparallel to chondrule long shape axes (Figures 1 and 2). Further details are provided in File S1.

When the shape alignments are extracted from SEM images (i.e., from 2-D planar sections), it is not possible to determine whether they are foliation or a lineation fabric in 3-D. However, given that all petrofabrics observed in 3-D μCT data were foliation textures (Figure 1, Table S1, File S2), the fabrics observed in thin sections are likely to be 2-D representations of 3-D foliations. Those samples that do not exhibit preferred orientations of chondrule long axes in 2-D may either be samples of random fabrics or the thin section has been cut parallel to the foliation plane.

## Macroscale Porosity

The macroscale porosity (voids >10 μm) of Winchcombe fragments, measured by μCT, ranged from

---

FIGURE 1. Representative μCT slices from chips of the Winchcombe meteorite and contoured orientation data on the long and short shape axes of chondrules plotted on a lower hemisphere stereographic projections and n denotes the number of chondrules measured for each plot. (a) Chip from BM.2022,M3,29 with a random texture and no preferred alignment of chondrule shapes. (b) Chip from BM.2022,M4,10 has a foliation texture with a girdle maxima in the long chondrule shape axis and a lineation texture in the short chondrule shape axis. (c) Chip from BM.2022,M2,34 has three lithologies. The projections reveal a foliation texture in two of the lithologies but the foliation planes of the two chips are in different orientations. (d) In the chip from BM.2022,M1,84, a pervasive set of parallel fractures pervade the lithology. The orientation of each fracture is plotted on a rose diagram confirming their parallel orientation.

**(a)** No fabric — BM.2022,M3,29 — Long axis, Short axis, n = 40

**(b)** Fabric — BM.2022,M4,10 — Long axis, Short axis, n = 20

**(c)** Multi-lithology — BM.2022,M2,34 — L₁, L₂; Long axis, Short axis; L₁ n = 30, L₂ n = 50

**(d)** Fracture network — BBM.2022,M1,84 — Fracture orientation, n = 50

**Legend:** Kamb contours in standard deviations — 6 (red), 4 (green), 2 (blue)

0.56% to 4.21% (King et al., 2022). In three sub-volumes of BM.2002,M2,34, fractures that cut across the whole section were observed. These cross-cutting fractures contained most of the porosity giving values of 1.5%–4.2%. The sub-volume that contained no cross-cutting fractures had the lowest porosity of 0.56%.

## Permeability Fluid Flow Modeling

Permeability modeling of four sub-volumes from 'BM.2022,M2,34' revealed anisotropy in three of them. These sub-volumes were permeable along a plane defined by the cross-cutting fractures (permeability ranged from $5.9 \times 10^{-13}$ m$^2$ to $3.3 \times 10^{-14}$ m$^2$) and had a permeability that tended toward zero perpendicular to that plane (Table S2). The orientation of fractures changed between sub-volumes, and consequently the orientation of the permeable plane varied (Table S2). The fourth sub-volume, which contained no cross-cutting fractures, had a very low permeability in all three measured directions (Table S2). The near-zero permeability values reflect a lack of interconnecting pores within the lithologies at the spatial resolution of the μCT data (0.85–1.2 μm voxel$^{-1}$).

## Mineralogy of Winchcombe's FGRs, Matrix, and TCIs

Lithologic descriptions and petrologic subtypes have already been provided by Suttle et al. (2022). Therefore, the following will only cover additional descriptions of the matrix TCIs and FGRs, in order to understand heterogeneities in the degrees of aqueous alteration both within and between lithologies in the Winchcombe meteorite. Additional detailed observations are found in the File S1 and Figures S1–S3. Here we define FGRs as accumulations of fine-grained materials surrounding an inclusion such as a chondrule, altered chondrule, CAI, TCI, etc. The term TCI describes objects that contain fibers of tochilinite intergrown with cronstedtite (Fuchs et al., 1973; Pignatelli et al., 2017; Rubin et al., 2007; Tomeoka & Buseck, 1985; Vacher et al., 2019). However, TCI is a term that has been used to describe a variety of objects in CM chondrites, including many that contain no cronstedtite. The majority of TCIs in Winchcombe are type II (Suttle et al., 2022). Here we use "TCI-like objects" as a term for any object that is rimmed by and/or has fibers of an Fe-S-rich secondary phase, such as tochilinite with a Mg-rich core that contains a Mg-rich secondary phase, for example, Mg-rich serpentine. TCI-like objects can also contain carbonate or anhydrous silicates in their interior as well as void space. Our definition of TCIs is in line with the previous descriptions of TCIs in the literature (Fuchs et al., 1973; Pignatelli et al., 2017; Rubin et al., 2007; Tomeoka & Buseck, 1985; Vacher et al., 2019) but contains the caveat that these objects do not necessarily need to contain cronstedtite. Matrix is the remaining fine-grained interstitial material. The matrix may contain small fragments of TCI-like objects, FGR, chondrules, and CAIs. Note "Mx" is used throughout to define the cataclastic matrix between lithologies and matrix is used to describe the fine-grained inter-chondrule material within lithologies including the cataclastic matrix (Mx).

### Matrix

#### Matrix Composition

The chemical composition of matrix within each lithology is highly heterogeneous, consistent with previous work (McSween Jr, 1979a; Zolensky et al., 1993). In addition, the quantitative EDS data presented here were collected with a focused electron beam with a spot size of <1 μm rather than the defocused electron beam that has been used in previous EPMA-WDS works (McSween Jr, 1979a; Zolensky et al., 1993). As such, we might expect to observe a greater degree of chemical heterogeneity than in previous work on CMs, due to the smaller interaction volume and beam diameter the EDS signal is generated from in this study.

The data fields of the matrices of most lithologies overlap significantly. The average atom% Mg# of the matrix of each lithology overlaps within one standard deviation, with the exception of lithology B in section P30552 (Table 1; Figures 3b and 4b). All lithologies show a wide range of Fe, S, Mg, and Si + Al values that overlap with each other (Figures 3 and 4, Figures S4 and S5), but there are subtle variations in composition between lithologies that are described in detail in File S1. No correlation is observed between petrologic type and the Mg# or S concentration of the matrix of any lithology.

FIGURE 2. 2-D analysis of the preferred shape orientation of chondrules from SEM images of Winchcombe thin sections. (a) P30552 (lithology A), (b) P30542 (lithology B and fusion crust), (c) P30545 (lithology B and Mx), (d) P30424 (lithology B and Mx), (e) P30423 (lithology C), (f) P30541 (lithology D and Mx), (g) P30548 (Lithology E), and (h) P30540 (lithology F, G, and Mx). Chondrules and chondrule pseudomorphs are colored blue, CAIs yellow, and matrix gray. Lithological boundaries are marked in white lines and the boundary between areas affected by cracking from the fusion crust are demarked by red lines. The long shape axes of chondrules were plotted on a rose diagram and subdivided by lithology where multiple lithologies were present. Data show that most lithologies in the Winchcombe meteorite exhibit a preferred orientation of the long shape axes of chondrules.

*Matrix Petrology*

Detailed descriptions of the matrix mineralogy can be found in File S1. Here we summarize the pertinent observations and variations in the matrix between lithologies.

The matrix material across all lithologies is predominantly composed of fine-grained (1–5 μm) to coarse-grained (5–10 μm) clumps or laths of serpentine with interspersed tochilinite crystals and TCI-like object fragments (Figure 5a,b). Minor components of matrix are carbonates and magnetite. Rare phases such as daubréelite, schreibersite, eskolaite, refractory metal nuggets, and apatite have also been observed in individual lithologies, but their scarcity means it is not clear whether they are unique to those lithologies or just uncommon (Figure 5c–f).

In lithology A (CM 2.2), some regions of matrix appear to penetrate TCI-like objects as veins that run along grain boundaries and taper to a termination within the TCI-like object (Figure 6b). Serpentine laths within these veins have a consistent orientation. In Lithology A, one chondrule, close to the fusion crust, contains cross-cutting veins and infilled fractures of alteration products (Figure 7a,b). An early vein of serpentine is cross-cut by a later fracture filled with matrix (Figure 7a,b). These serpentine veins are curved, crystallographically controlled, and cut across forsterite, with crystals oriented parallel to vein margins. The serpentine veins are cross-cut by an iron-rich, matrix-filled fracture, which mostly consists of an amorphous silicate. The amorphous nature of the silicate was inferred due to non-stochiometric compositions and a lack of crystal boundaries. However, in some parts of the infilled fracture sheet-like crystals are observed, which are likely to be cronstedtite (Figure 7b).

In lithology B, the matrix is highly porous (12%) and contains a bimodal distribution of fine-grained (1–5 μm) and coarse-grained (5–10 μm) serpentine laths (Figure 5b). The matrix of lithologies B, E, and F is dominated (>60%) by TCI-like object fragments. Conversely, the matrix of lithology C comprises approximately 90 area % (Figure 2e), the remainder is comprised of dispersed TCI-like objects. The matrix of lithology D is distinct as it also contains partially altered metal grains. However, it should be noted that it is possible these metal grains could be carbides due to the challenges associated with detecting carbon by EDS (Brearley, 2021). Similarly, the matrix of lithology G is distinct as it contains several fragments of anhydrous silicates. Finally, the matrix of Mx is full of quasi-rectangular voids and is comprised of mainly coarse-grained (<20 μm) serpentine, with patches of fine-grained material adjacent to serpentine-rich regions.

*TCI-Like Objects*

*Composition of TCI-Like Objects*

WDS-EPMA/EDS data were acquired from the Mg-rich interior of TCI-like objects and their Fe-rich rims and fibers: in most cases, the Fe-rich phase is tochilinite and the Mg-rich phase is serpentine. Only data for TCI-like objects hosted in the matrix are presented here. Data for TCI-like objects in chondrules and chondrule pseudomorphs are presented separately in this paper. In addition, as the Fe-rich fibers are thin and intergrown with Mg-rich serpentine, many data points from the TCI-like object rims are likely mixtures of the Fe-rich tochilinite fiber and the Mg-rich serpentine core due to the interaction volume from which the x-ray signal was generated. However, our use of a focused electron beam here means that we have a reduced impact from contributions from this nanoscale heterogeneity than from a defocused electron beam and are able to resolve heterogeneities in TCIs at a greater spatial resolution.

The composition of all Mg-rich cores of the TCI-like objects in all lithologies is relatively uniform (Figures 3 and 4 Figures S4 and S5, Table 1). In particular, the average Mg# is indistinguishable within two standard deviations for all lithologies except lithology E, which has a slightly lower Mg# (Figure 4, Figure S5, Table 1). There are subtle chemical differences that are presented in File S1.

The composition of the Fe-rich tochilinite rims of the TCI-like objects covers a broad wedge in the atom% ternary plots that taper toward the composition of the Mg-rich serpentine core cluster (Figure 3, Figure S4). Although there is some overlap, each lithology seems to have distinct TCI-like object rim compositions (Figure 3, Figure S4). Specific differences are presented in File S1. Lithology Mx spans the full range of compositions (Figures 3 and 4, Figures S4 and S5). However, the overlap of lithology Mx TCI-like object rims is not complete, particularly for Mg#. No correlation is observed between each lithology's petrologic type and Mg# or S abundance in the TCI-like object's rims.

*Petrology of TCI-Like Objects*

TCI-like objects have been described in detail across the lithologies in the Winchcombe meteorite by Suttle et al. (2022) and are in general consistent with descriptions of TCIs in the literature (Fuchs et al., 1973; Pignatelli et al., 2017; Rubin et al., 2007; Tomeoka & Buseck, 1985; Vacher et al., 2019). Here we briefly provide additional descriptions of TCI-like objects relevant to the present study. Detailed descriptions can be found in File S1.

In general, TCI-like objects occur as large 20–200 μm clumps in the matrix and approximately half are enclosed by FGRs (Figures 6g, 8a,h and Figure S1). In lithology A
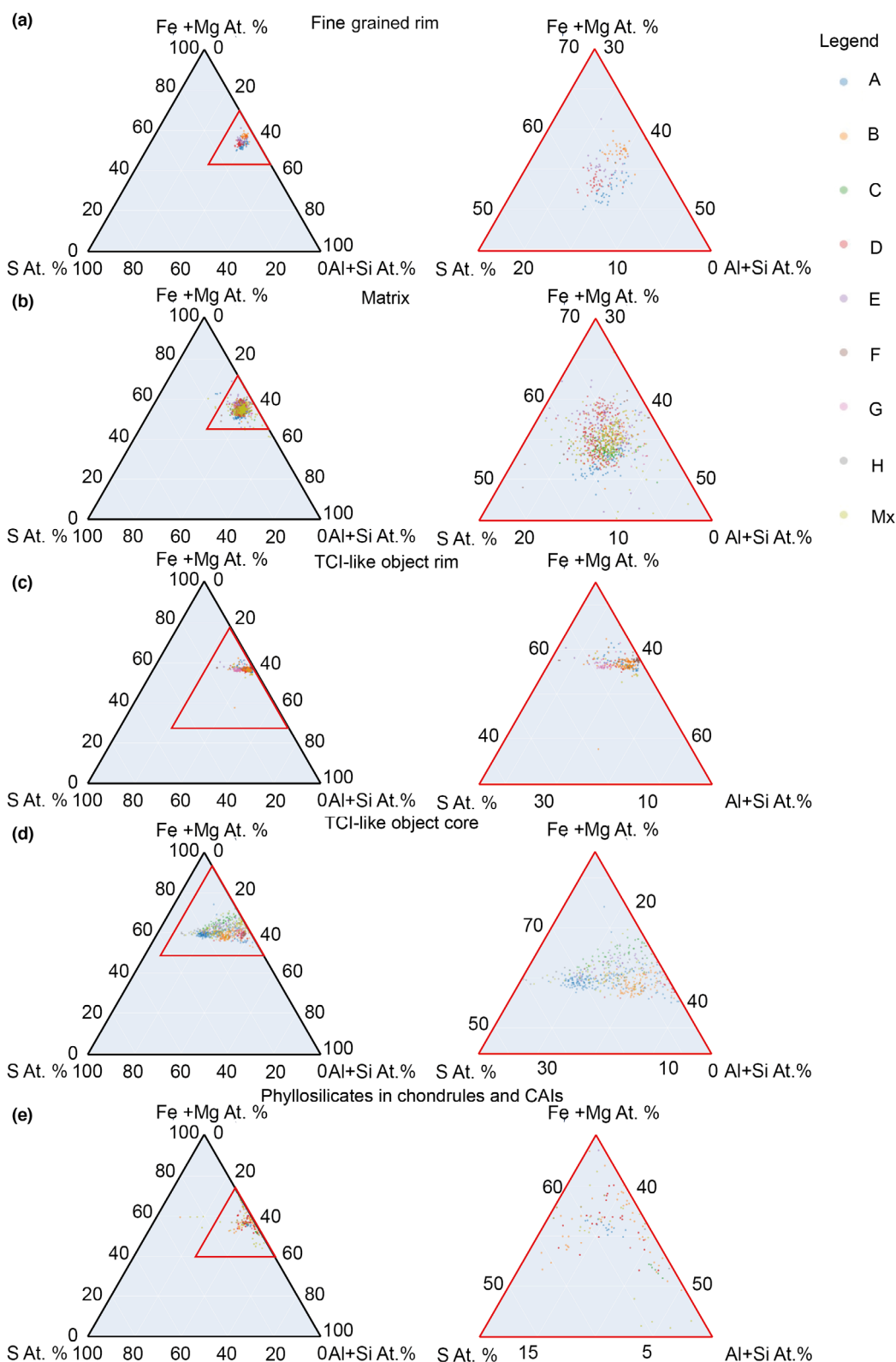
FIGURE 3. Ternary plots (atom%) of Fe + Mg versus S versus Al + Si measured by WDS-EPMA and EDS of (a) fine-grained rim, (b) matrix, (c) TCI-like object rim, (d) TCI-like object core, and (e) phyllosilicates in chondrules and CAIs. Colors are used to distinguish EDS and WDS-EPMA measurements from different lithologies. The red triangle on the ternary on the left hand side indicates the limits of the magnified view of the ternary presented on the right.
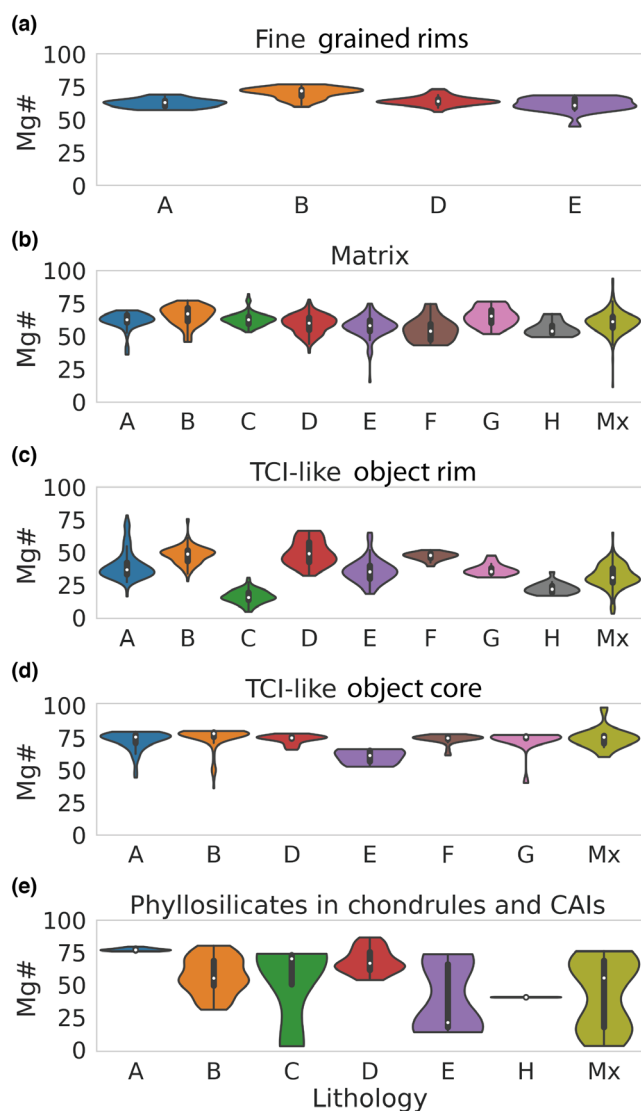
FIGURE 4. Violin plots of Mg# (atom%) versus lithology from WDS-EPMA and EDS measurements of (a) fine-grained rim, (b) matrix, (c) TCI-like object rim, (d) TCI-like object core, and (e) phyllosilicates in chondrules and CAIs. Violin data distributions are constrained by the limits of the measured data.

and B, TCI-like objects cover ~30%–40% of the area of the meteorite (Figures S1 and S2). In lithology C, TCI-like object abundance is reduced to 10 area % and they are absent from lithology D (Suttle et al., 2022) (Figure S3a,b respectively). TCI-like objects dominate the inter-chondrule space in lithology F (Figure S3d). In lithology Mx, TCI-like objects appear as rounded clusters (Figure S3b,d,f).

Approximately 30% of TCI-like objects have drusy textures exhibiting tochilinite crystals decorating the external surface of the inclusion with a core of serpentine/cronstedtite (Figures 6g, 8a,h and Figure S1).

The central area of some TCI-like objects includes void space or calcite/aragonite (Figure 6f and Figure S1). Many TCI-like objects have angular outlines and are present in clusters of objects with seemingly related textures, except in lithology Mx where they are more rounded (Figures S1–S3). Where TCI-like objects occur as a cluster, the surfaces of many of the TCI-like objects are separated by areas of matrix and have matching geometries (on the plane of section) (Figure 6b and Figure S1). Between these TCI-like objects are broadly tabular shaped areas of matrix that penetrate a single TCI-like object and taper to a termination within them (Figure 6b,g). In one of the areas where veins of matrix have penetrated between TCI-like objects, the coarse serpentine crystals in the matrix have a consistent shape orientation (Figure 6b).

Low kV, high vacuum, and ultra-high spatial resolution EDS maps show four distinct phases within drusy TCI-like objects: two Mg-rich phyllosilicates, where one contains moderately more Fe than the other, and two Fe-rich phyllosilicates with different Fe contents (Figure 6g). The moderately Fe-rich phyllosilicates occur as symmetrical veins, with an Mg-rich core, that are faceted and penetrate in from the edge of the inclusion and then curve toward the interior of the TCI-like objects to meet at 120° triple junctions (Figure 6g). On the exterior of the TCI-like objects these veins are split along the central point by microfractures (Figure 6g). The most Fe-rich phyllosilicates occur as straight to curved fibrous growths that extend from the moderately Fe-rich veins into the Mg-rich region (Figure 6g). Both phases that contain moderate amounts of Mg or are Mg rich occur as patches that infill the area between the Fe-rich fibers and veins (Figure 6g).

FIB-TOF-SIMS analysis of drusy TCI-like objects reveals that Na is enriched within the region containing the Fe-rich fibrous phyllosilicates and Ca is enriched at the termination of the Fe-rich serpentines (Figure 8a–e).

TEM analysis of these drusy TCI-like objects revealed that they are comprised of tochilinite–serpentine fibers enclosed by Mg-Fe serpentine (Figure 8f,g). The Mg-Fe phyllosilicates have a fine lamellar structure and are crystallographically aligned with the tochilinite fiber. The Mg-rich interior of the TCI-like objects is also porous with pores aligned perpendicular with the orientation of phyllosilicate fibers (Figure 8f,g). The $d_{001}$-spacings range 0.66–0.74 nm, averaging ~0.70 nm, with repeating units of two layers, consistent with 1:1 layered T–O phyllosilicate, characteristic of serpentine-group minerals. APT analysis of a similar drusy TCI-like object (Figure 8h) reveals fine interlaminations of Fe-rich and Mg-rich phyllosilicates, and Na is concentrated on the boundaries between these two phases (Figure 8i,j).
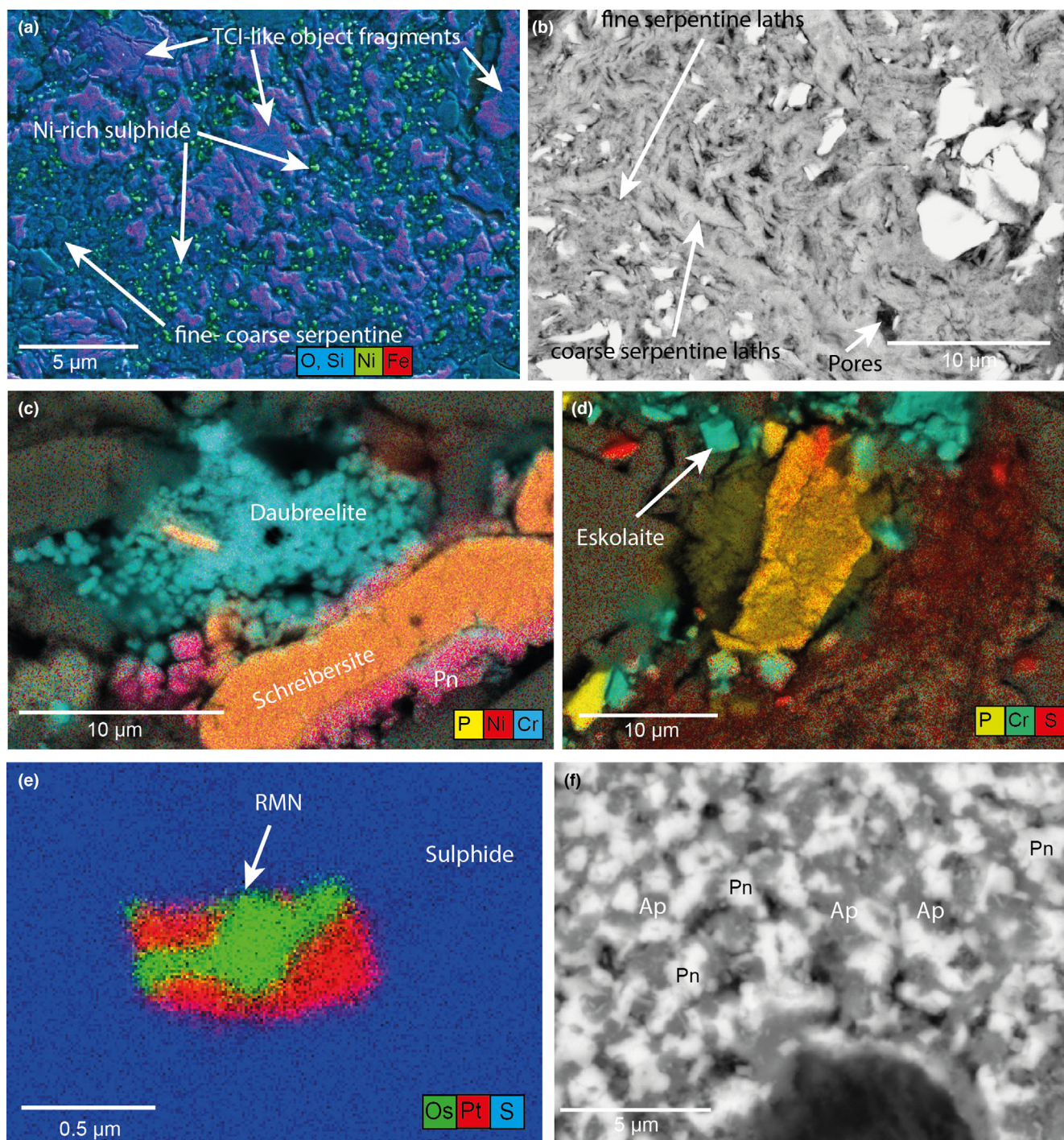
FIGURE 5. EDS maps and BSE images of fine-grained minerals and materials within the Winchcombe meteorite. (a) Low voltage (3 kV) EDS map of the matrix of lithology A, showing fine-grained serpentines, fragments of TCI-like objects, and Ni-sulfides. (b) BSE image of the matrix of lithology B revealing high-porosity and fine- to coarse-grained serpentine laths and sulfide grains (bright phases). Both the pores and serpentine laths have a preferred orientation with the long shape axis running top left to bottom right of the image. (c) EDS map of schreibersite, daubréelite, and pentlandite (Pn) within lithology A. (d) EDS map of eskolaite and P-bearing sulfides within lithology F. (e) EDS map of a refractory metal nugget within a sulfide grain within the matrix of lithology E. The RMN is multi-domain with Pt-rich and Os-rich regions. (f) BSE image of fine-grained intergrowths of apatite (Ap) and pentlandite (Pn) within lithology F.
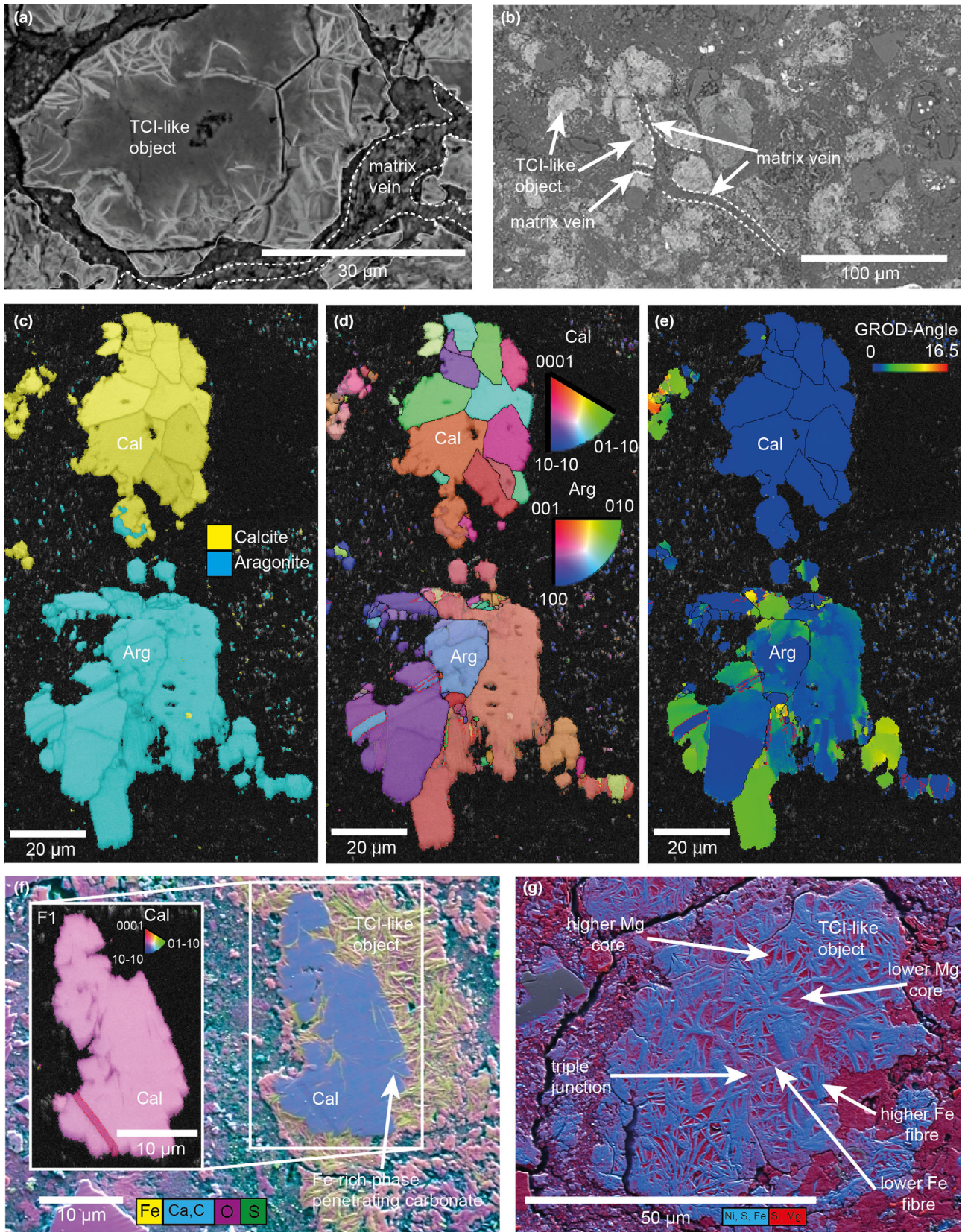
FIGURE 6. EDS-EBSD maps and BSE images of the range of carbonate to TCI-like object replacement textures present in the Winchcombe meteorite lithology A. (a, b) BSE images of a TCI-like objects that have been displaced and disrupted by veins of matrix that penetrate along grain boundaries in the TCI-like object and taper to a point. The matrix veins are highlighted by the white dashed lines. (c) EBSD phase map showing two carbonate grains, one aragonite (Arg), and the other calcite (Cal). At the bottom of the Cal grains is an inclusion of Arg. (d) EBSD Inverse pole figure map of the same Cal Arg assemblage as in (c) showing the orientation of Arg and Cal crystals. The grain boundaries are perpendicular to the grain edge and curve to 120° triple junctions within the carbonate grains and the Arg exhibits mechanical twins highlighted by red lines. The grain shapes are otherwise similar between Cal and Arg. In addition, where the Arg and Cal are present in the same location, the IPF color is similar suggesting a crystallographic orientation relationship and epitaxial replacement. (e) EBSD Grain Reference Orientation Deviation (GROD) angle map of the same Cal-Arg assemblage as in (c) showing the misorientations of Arg and Cal crystals. The misorientation of pixels from the average orientation of that grain is color coded, where blue is low misorientation and green-yellow express higher amounts of misorientation. Cal is completely undeformed and Arg displays extensive internal misorientation. Twin boundaries in the Arg are highlighted by red lines. (f) EBSD and low voltage (5 kV) EDS map of a Cal grain that has been partially replaced by a TCI-like object. Note that the Fe-rich fibers of the TCI-like object are straight when they penetrate the Cal and appear to be following cleavage and grain boundaries. (g) Low voltage (5 kV) EDS map, of a TCI-like object. The TCI-like object contains two Fe-rich phases that are present as fibers that both surround and penetrate into the TCI-like object and two Mg-rich phases that are present in the core of the TCI-like object. Of the two Fe-rich phases, the most Fe-poor variety has a very similar texture to the grain boundaries exhibited in calcite and aragonite phase that are perpendicular to the edge of the object and bent into 120° triple junctions in the interior of the TCI-like object, suggesting a pseudomorph texture.

## Fine-Grained Rims

### Composition of FGRs

Both EDS/WDS-EPMA data were only acquired for FGRs in lithologies A, B, D, and E (Table 1, Figures 3 and 4, Figures S4 and S5). As before, a focused electron beam was used and as such, we might expect to see a greater degree of heterogeneity compared to previous studies that used a dispersed beam due to the reduced electron beam interaction volume. All these lithologies exhibit a wide scatter of compositions (Figures 3 and 4, Figures S4 and S5). Lithology D and E compositional data broadly overlap (Figures 3 and 4, Figures S4 and S5). Lithology B FGRs appear to be compositionally distinct (with relatively higher Mg contents) from those of A, D, and E, though there is some overlap toward the higher Fe compositions of lithology B (Figures 3 and 4, Figures S4 and S5). More details are provided in File S1.

### Petrology of FGRs

In all lithologies, FGRs occur as mantles around objects like chondrules, silicate fragments, and TCI-like objects. The FGRs in Winchcombe are similar to FGRs described for CMs in the literature (Chizmadia & Brearley, 2004, 2008; Lauretta et al., 2000; Metzler et al., 1992; Noguchi et al., 2021; Pinto et al., 2022; Zanetta et al., 2021) and as such, only relevant observations for this study are presented here. FGRs exhibit a homogeneous, compact texture (no layering), have a relatively uniform thickness (typically 30–100 μm), and are similar to the matrix in petrographic appearance, independent of what object they are mantling. One exception is the Mx, where one large chondrule has a wide FGR with distinct layers—compact next to the chondrule edge and porous in an outer layer.

At the TEM scale, the FGRs are composed mainly of finely crystalline material whose selected area diffraction (SAED) patterns contain continuous rings with d-spacings of 0.45, 0.36, 0.25, and 0.15 nm; this material characteristically has ≲100 nm diameter pores (Figure 9a,b). There are also micrometer-sized irregular areas, patches or bands within the FGRs that are more coarsely crystalline (Figure 9a,b), and high-resolution TEM images show that constituent nanocrystals have a ~0.72 nm lattice fringe spacing indicative of serpentine (Figure 9a). The coarsely crystalline areas yield SAED patterns containing sectored rings that have d-spacings of 0.35, 0.25, and 0.13 nm.

Constituents of the FGRs also include organic nanoglobules a few hundred nanometers in diameter (Figure 9b,c). Some of the nanoglobules are hollow, and some are partially embayed by the finely crystalline material (Figure 9b,c). The FGRs also contain objects ~3 μm in size that are distinguished by the presence of euhedral crystals of sulfide and/or Fe-Cr-oxides that typically are ≲200 nm in size but can reach up to ~800 nm (Figure 9d–f). These objects also contain some thin filaments of serpentine (Figure 9d–f). They are hereafter referred to as nano-sulfide/oxide objects (Figure 9d–f). The constituent sulfide/oxide crystals are enclosed within amorphous material that stands out from surrounding phyllosilicates by a compact structure and the absence of nanopores (Figure 9d–f). Most of the crystals were too small to chemically analyze by TEM, but the largest crystal in Figure 9f is a Fe-Ni sulfide.

## Carbonate Textures

Several lithologies contain carbonate phases including calcite, dolomite, and aragonite that are associated with
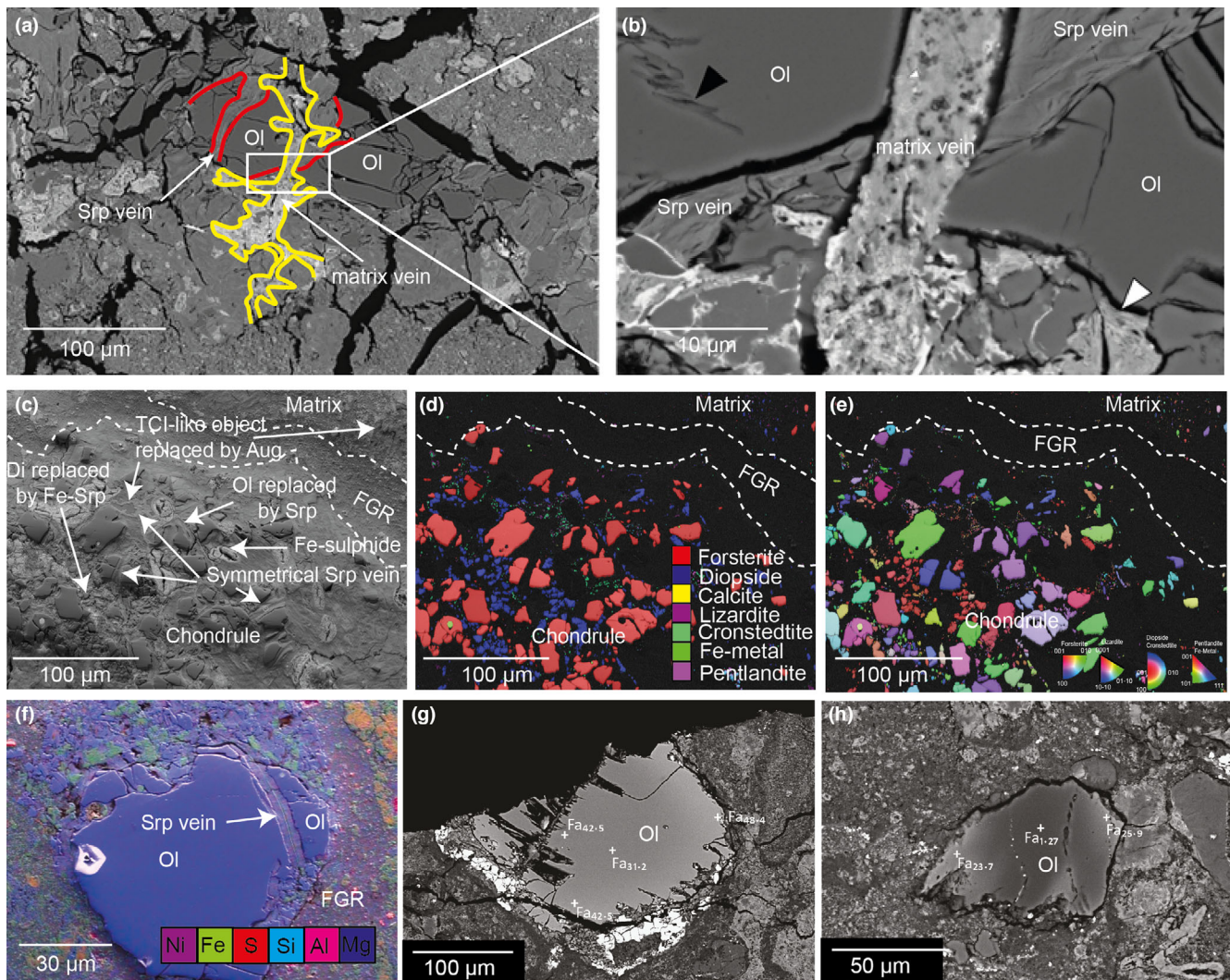
FIGURE 7. BSE images and EBSD maps of the range of replacement textures observed in anhydrous silicates in Winchcombe. (a, b) are BSE images of cross-cutting veins of matrix material that have penetrated into olivine (Ol) grains, cutting across both the Ol and serpentine (Srp) veins. The red lines outline the boundary between Srp and Ol and the yellow lines outline the boundary between a vein of matrix and Ol. Again, no alteration is observed where hydrated matrix is in contact with Ol. (c–e) BSE, EBSD phase map, and EBSD IPF map, respectively, of anhydrous silicates in a chondrule. BSE images show that the Ol grains are partially replaced by Srp which is both penetrating along subgrain boundaries and replacing the exterior of the Ol crystals. The Srp trends from Fe-rich at the center of the vein to Mg-rich in contact with Ol. Diopside (Di) is also partially replaced by phyllosilicates. There are also TCI-like objects within the chondrule that have completely replaced the precursor phase—likely Augite (Aug) orthopyroxene. EBSD shows that the Fe-rich phase is a mixture of cronstedtite and lizardite, and the IPF maps show that these have similar orientations along edges of the TCI-like object suggesting a relationship between the secondary phase and the primary phase. The white dashed line outlines the boundaries of the fine-grained rim. (f) EDS map of an Ol clast in the matrix of lithology A. Here the exterior of the Ol grain is unaltered and only a crystallographically controlled Srp veins are observed that dissects the Ol. There is a cross-cutting relationship where the Srp vein is truncated by a vein of matrix, and the Ol does not show evidence of alteration where in contact with the hydrated matrix material. (g, h) BSE images of Ol grains that have Fe-rich rims. The Fe-rich Ol is unaltered to partially altered, even where in contact with hydrated matrix.

TCI-like objects (Figure 6 and Figure S6) and are similar to TCI-hosting carbonates described in the literature (Dobrică et al., 2022; Lee et al., 2012; Lindgren et al., 2017). Observations relevant to the interpretations are outlined below and detailed descriptions can be found in File S1.

EBSD microanalysis show that both calcite and aragonite are present within lithology A (Figure 6c–f). Aragonite clusters contain several discrete grains with faceted grain boundaries that align with crystallographic axis and meet at 120° triple junctions (Figure 6c–f). Aragonite grains show extensive crystal plastic

deformation microstructures including mechanical twins (some of which are curved), intragranular disorientation, and subgrains (Figure 6e). The subgrains within aragonite have faceted shapes. Intragranular low-angle boundaries show clear rotation about <100>, and Weighted Burgers Vectors preferentially parallel to <001> and <010>. These microstructures are consistent with deformation by dislocation creep. Conversely, calcite is completely undeformed. However, in common with aragonite, it has multigrain assemblages with the same faceted grain boundaries that align with crystal axes and meet at 120° triple junctions (Figure 6c–f). Aragonite and calcite can also be found within the same carbonate assemblage, where they exhibit an epitaxial relationship where the major crystal axes of aragonite and calcite are in the same orientation (Figure 6d).

Calcite is also observed to be partially replaced by TCI-like object material (Figure 6f). These replacement textures are similar to literature descriptions of carbonates in CMs (Dobrică et al., 2022; Lee et al., 2012; Lindgren et al., 2017). Interestingly, some TCI-like objects that do not contain residual calcite also exhibit similar textures to the unaltered calcite and aragonite grains, with straight grain boundaries and 120° triple junctions defined by Fe-S-rich phyllosilicates (Figures 6a, b,g and 8h).

## Anhydrous Silicate Alteration Textures

Whole section EDS maps where Mg is red, Fe is green, and Ca is blue are ideal for visualizing the distribution of olivine and pyroxene (bright red), serpentine (dark red), carbonate (blue), and TCI-like objects (green). These maps reveal that within all lithologies, except lithology F (Figure S3a), anhydrous silicates including olivine and pyroxene occur (Figures S1–S3). The distribution of surviving olivine grains in both chondrules and as fragmented grains in the matrix is random (Figures S1–S3). No relationship is observed between the concentration of surviving olivine grains and any 2-D petrofabric, nor do certain areas within the same lithology contain higher or lower abundances of olivine (Figure 2, Figures S1–S3). Chondrules that are completely altered to secondary mineral assemblages are situated close to or even touching chondrules that contain surviving olivine. However, all surviving anhydrous silicates exhibit some evidence of aqueous alteration. EBSD and EDS reveal that Fe-Ni metal grains are preserved in some anhydrous silicates that have been protected from aqueous fluids (Figure 7d). In lithology D, there is ~1.5% metal including metal grains that are not enclosed within anhydrous silicates, a testament to its low alteration extent. Large metal grains can also be found in chondrule olivine from the Mx lithology.

There is an apparent difference between the extent of aqueous alteration of chondrule-hosted and matrix-hosted anhydrous silicates in some lithologies. Chondrule-hosted anhydrous silicates, both pyroxene and olivine (Figure 7c–e), are more extensively altered than their matrix counterparts (Figure 7f–h). Chondrule olivine and pyroxene grains exhibit alteration textures around all exterior surfaces (Figure 7c–e), as well as symmetrical crystallographically controlled alteration veins of phyllosilicates that cut across the olivine crystals (Figure 7c–e). In contrast, alteration textures in matrix olivine grains are not present on all exterior surfaces, and cross-cutting relationships are observed between interior alteration veins and the surrounding FGRs or matrix material (Figure 7g, h). Some matrix-hosted olivine grains in lithology B exhibit Fe zoning with classic diffuse Fe-rich rims (Figure 7g, h). These Fe-rich olivine rims show little to no evidence of being preferentially altered to serpentine (Figure 7g,h).

EBSD analysis of both partially altered chondrule- and matrix-hosted olivine and pyroxene grains/fragments in lithology A reveals that they are undeformed, with no internal misorientation observed on either side of alteration vein structures (Figure 7c–e). However, many chondrules are fragmented and are not spherical but elongate (Figures 1 and 2, Figures S1–S3). Two phyllosilicate phases were detected by EBSD within a single partially altered chondrule (Figure 7c–e). These diffracting phyllosilicates were found on the outer rim of discrete alteration assemblages, with a Fe-rich rim that is straight or zig zagged with a Mg-rich core (Figure 7c–e), similar to objects described in other CMs (Hanowski & Brearley, 2001; Velbel, 2014; Velbel et al., 2012, 2015). These crystalline phases are consistent with cronstedtite and lizardite (Figure 7c–e). Within these diffracting phyllosilicate alteration assemblages, none of the original phase survives; the cronstedtite and lizardite exhibit symmetrical vein textures and appear to have completely replaced the preexisting mineral (Figure 7c–e). In some regions, there appears to be a crystallographic orientation relationship between cronstedtite and lizardite, where along straight portions of the vein the phases have a consistent orientation (Figure 7e). Cronstedtite and lizardite are only detected in the Fe-rich rim surrounding an Mg-rich core of these alteration assemblages (Figure 7c–e). The phyllosilicate assemblages that still surround or are within surviving chondrule olivine and pyroxene, do not yield any diffraction patterns, have higher S and Ni and lower Fe compositions and a different morphology to the secondary alteration phases that yielded diffraction patterns (Figure 7c–e). The lack of diffraction patterns from the alteration phases surrounding olivine could be because they are nano crystalline, producing a mixed diffraction pattern. We do not believe that poor sample preparation or beam
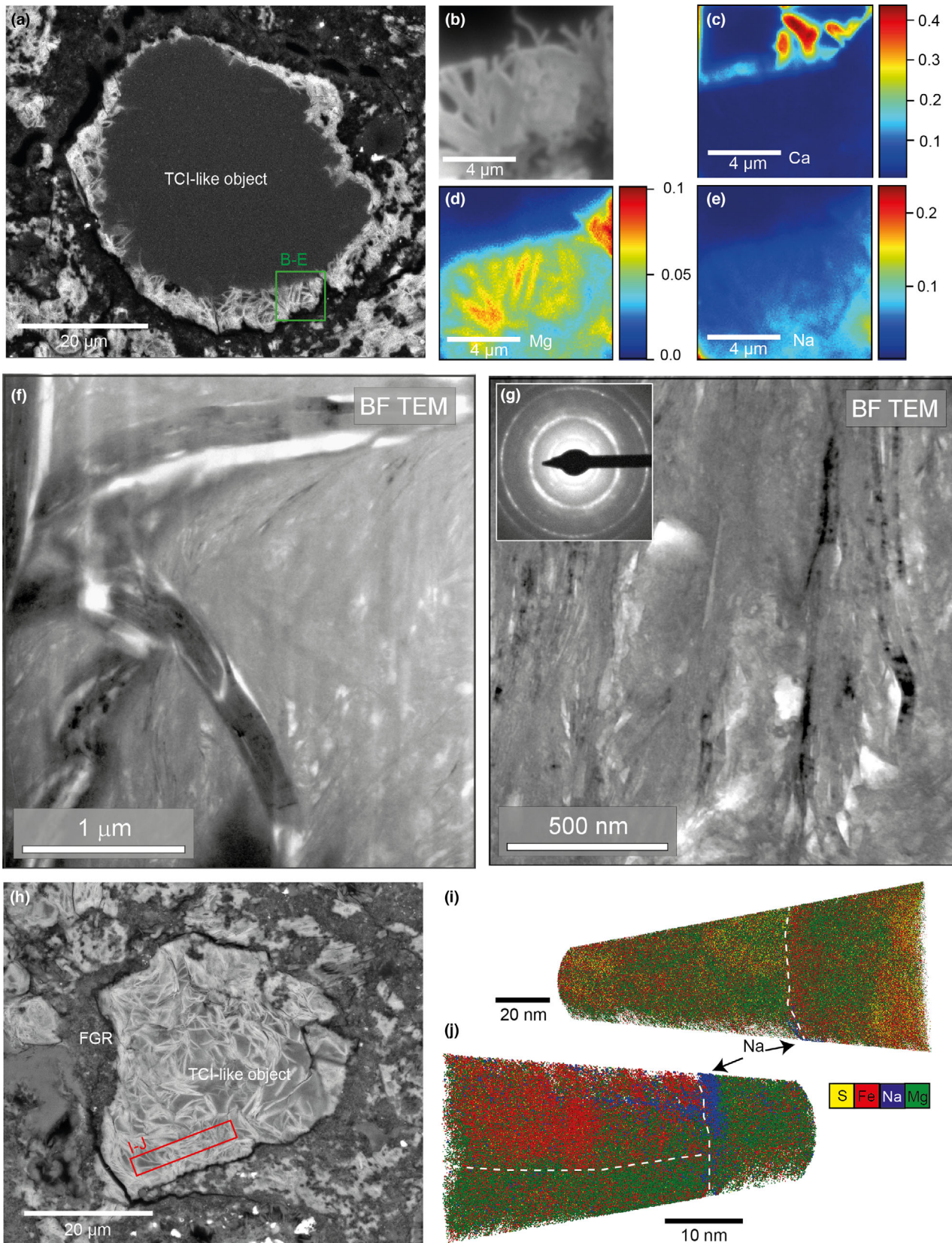
FIGURE 8. BSE, FIB-TOF-SIMS, and APT data of the interface between the Fe-rich and Mg-rich phases in TCI-like objects from lithology A. (a) A BSE image of a TCI-like object surrounded by a FGR; the green box shows where the FIB-TOF-SIMS maps were acquired from. (b–e) FIB-TOF-SIMS maps showing SE, Ca, Mg, and Na distributions respectively. Na is concentrated in the Fe-rich fibers and Ca is concentrated on the boundary between Fe- and Mg-rich regions. (f, g) TEM bright field images of TCI-like object rims and fibers panel G also has an inset SAED pattern. (h) BSE image of a TCI-like object surrounded by a FGR, the red box indicates where APT samples were extracted from. (i, j) APT data sets of the intergrowth of Fe- and Mg-rich showing the distribution of Fe, Na, Mg, and S atoms revealing that Fe- and Mg-rich phases are intergrown at the nanoscale and Na is concentrated at the boundaries between phases. The dashed line highlights the boundary between the Fe- and Mg-rich phases.

sensitivity of the phases is a likely reason for the lack of diffraction patterns as lizardite and cronstedtite also require near perfect sample preparation and are highly beam sensitive (Daly et al., 2020, 2021; Lee et al., 2003).

The geochemistry of alteration mineral assemblages of phyllosilicates within chondrules, CAIs, and clasts of anhydrous silicate is largely similar to that of the matrix, FGR, and TCI-like object compositions, but phyllosilicates in chondrules have much lower concentrations of S consistent with Hanowski and Brearley (2001) (Table 1, Figures 3 and 4).

## DISCUSSION

### Macroscale Brecciation of the Winchcombe Meteorite

Brecciation and reaccretion is an important process that affected many CM chondrites (Bischoff et al., 2017; Lee, Floyd, et al., 2023; Lentfort et al., 2021; Lindgren et al., 2013). Brecciated CMs contain distinct CM lithological clasts juxtaposed with other CM clasts generally with different textures, proportions of chondrules matrix and TCI-like objects and aqueous alteration histories (Bischoff et al., 2017; Lee, Floyd, et al., 2023; Lentfort et al., 2021; Lindgren et al., 2013). Some clasts can have their own smaller discrete clasts present within them (Lentfort et al., 2021). The Winchcombe meteorite is also a breccia with eight distinct lithologies with different aqueous alteration histories spanning petrologic types CM2.0–2.6 that are suspended within a cataclastic Mx (Suttle et al., 2022). Noble gas measurements of Winchcombe show it is from the regolith near the surface of its parent asteroid (King et al., 2022). As such, brecciation has clearly played an important role in the evolution of this meteorite as it does for most CM meteorites.

It is generally thought that brecciation occurred late, after the cessation of aqueous activity (Bischoff et al., 2017) and that each individual lithology was altered by fluids as a whole on discrete parts of a parent body (Brearley, 2003, 2006; Rubin et al., 2007; Suttle et al., 2021). There is some evidence that some aqueous alteration occurred after brecciation, that is, the

preservation of iron-rich haloes in some CM chondrites, or that some CMs escaped brecciation preserving these delicate aqueous alteration textures (Hanowski & Brearley, 2000). Regional planetesimal scale aqueous alteration will largely overprint and obscure earlier nebular and accretionary processes (Brearley, 2006; Weisberg et al., 2006), as well as homogenize secondary mineral chemistry (Brearley, 2006). Water–rock reactions in particular result in relatively quick (days-months-years) (Andreani et al., 2013; Jones & Brearley, 2006; Lafay et al., 2012; Lamadrid et al., 2017, 2021; Martin & Fyfe, 1970; Velbel et al., 2012) replacement of primary mineralogy with secondary minerals by dissolution and reprecipitation reactions (Pirajno, 2012; Putnis et al., 2009). These water–rock reactions rapidly converge to geochemical equilibrium, thus, assuming no change in physiochemical conditions of the fluid occurs, aqueous alteration produces a diverse secondary mineral assemblage, where each mineral constituent is geochemically uniform (Fulignati, 2020; Velbel, 2014; Velbel et al., 2012). However, if this assumption does not hold, then the secondary mineral assemblage will be diverse internally and locally also (Hanowski & Brearley, 2001; Singerling & Brearley, 2020).

Meteorites of the CM chondrite group have been affected by fluids to varying degrees (Brearley, 2003; Hewins et al., 2014; Lee et al., 2012, 2014; Lindgren et al., 2017; Metzler et al., 1992; Rubin et al., 2007; Suttle et al., 2021). As the severity of fluid alteration increases, a range of changes are observed:

1. Anhydrous silicates such as Mg-rich olivine become progressively replaced by phyllosilicates ranging from CM3.0 (unaltered anhydrous silicates) to CM2.0 (completely altered anhydrous silicates) on the Rubin et al. (2007) scale.
2. The Mg content of the matrix and other secondary minerals increases (McSween Jr & Richardson, 1977; Rubin et al., 2007; Suttle et al., 2021).
3. The Si content of TCIs increases (Rubin et al., 2007; Suttle et al., 2021).
4. Carbonates become more mineralogically complex with aragonite becoming replaced with calcite and then subsequently replaced with dolomite,
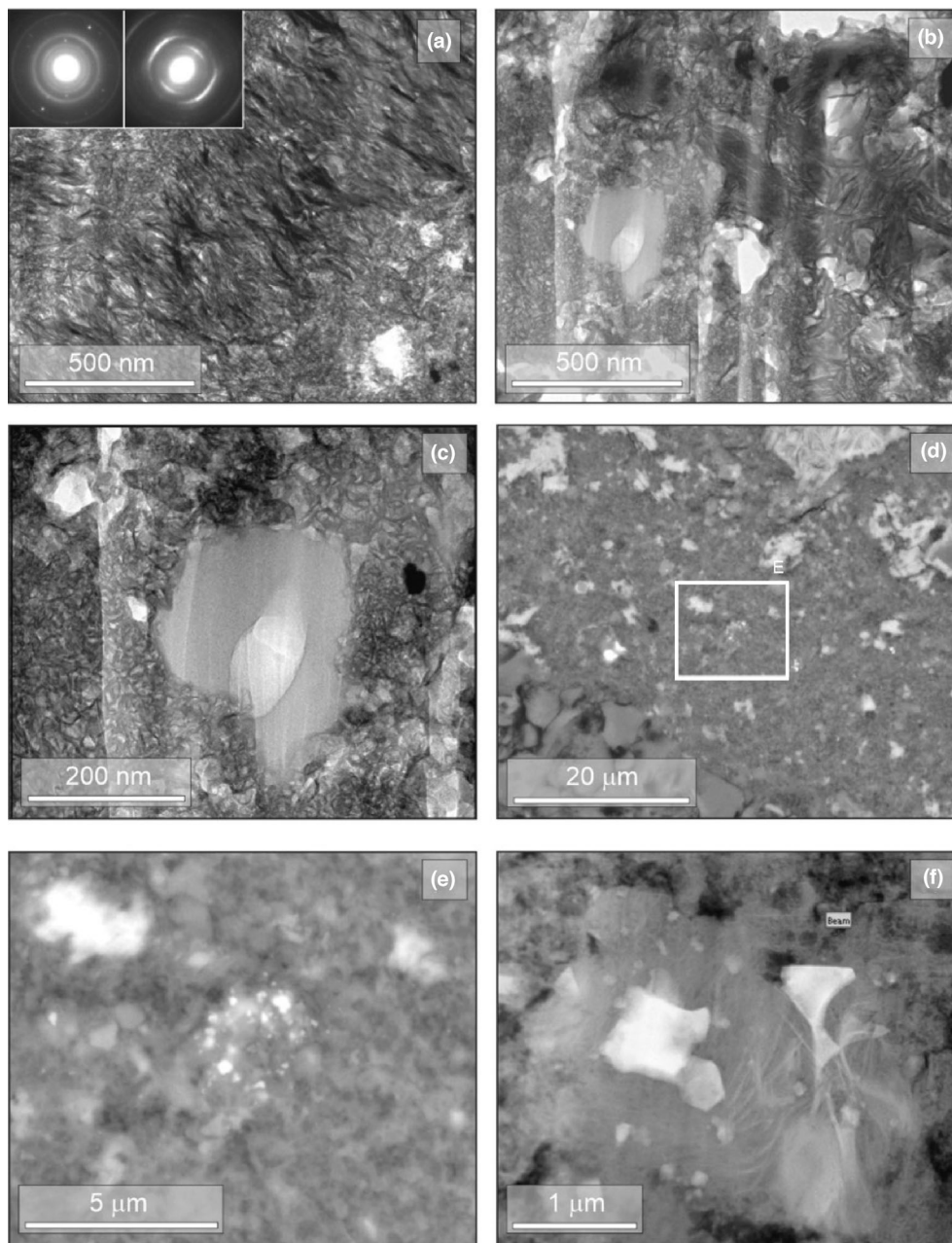
FIGURE 9. Fine-grained rims (FGRs) in Winchcombe lithology A. (a) Bright-field TEM image and inset SAED patterns. In the image is a band of relatively coarsely crystalline phyllosilicate (with fibers extending from upper left to lower right) surrounded by more finely crystalline and porous phyllosilicate (pores are white). The left-hand side SAED pattern is from an area of the finely crystalline phyllosilicate and shows that the constituent crystals and small and randomly oriented. The most prominent ring has a d-spacing of 0.26 nm. The SAED pattern to its right is from the more coarsely crystalline band, and the two most prominent sectored rings have d-spacings of 0.35 and 0.25 nm. (b) Bright-field TEM image showing an area of a different rim to (a) that also comprises patches of phyllosilicate that differ in crystal size. The finer grained phyllosilicate is again micropore-rich, and also contains a hollow organic nanoglobule. The vertical streaks are artifacts from FIB milling. (c) Bright-field TEM image of the nanoglobule in (b), the exterior parts of which have been partially replaced by the phyllosilicate. d) BSE image of a fine-grained rim on a chondrule, the outer edge of which can be seen in the lower left. (e) BSE image of the white boxed area in (d) showing an object 3 μm across that is an aggregate of sulfide and/or metal grains ~75–225 nm in size. (f) HAADF STEM image of an amorphous silicate grain with embedded nano-sulfide/oxide that is enclosed in a nanoporous phyllosilicate groundmass. Most of the sulfide/oxide grains are euhedral, and ~100–800 nm in size, and are supported within an amorphous matrix. The crystal to the left of center is a Fe-Ni sulfide.

breunnerite, and phyllosilicates (Lee et al., 2012, 2014; Lee & Ellen, 2008).

5. Destruction or modification of primary accreted materials that are typically more sensitive to the fluid, that is, amorphous silicates, organics, presolar grains, chondrule mesostasis, metal, primary sulfides, fayalitic olivine, and FGRs (Brearley, 2003, 2006; Hanowski & Brearley, 2001; Leroux et al., 2015; McSween Jr, 1979a; Metzler et al., 1992; Pinto et al., 2022; Rubin et al., 2007; Singerling & Brearley, 2020; Suttle et al., 2021; Tomeoka & Buseck, 1985; Zanetta et al., 2021, 2022).

In many CMs, these replacement reactions are not uniform as expected for whole-rock aqueous alteration, and observations of CM chondrites show substantial heterogeneity in the degree of aqueous alteration experienced by similar components not only between lithologies but also within them (Bischoff, 1998; Brearley, 2003; Leroux et al., 2015; Metzler et al., 1992; Zolensky et al., 1997). Some of this heterogeneity in secondary minerals can be reconciled if the effect of brecciation is accounted for (Hanowski & Brearley, 2001). Here, secondary mineral heterogeneity is controlled by the precursor phase and local microenvironments (Hanowski & Brearley, 2001). However, disequilibrium textures that cannot be reconciled by clast scale brecciation are widespread in CMs with nearly unaltered mineral grains near completely altered pseudomorphs of the same primary mineral (Bischoff et al., 2017; Metzler et al., 1992; Noguchi et al., 2021; Suttle et al., 2021; Zolensky et al., 1997). In Winchcombe, we see similar evidence for this heterogeneity in the response of CM components similar to aqueous alteration even in low petrologic subtypes (CM2.2–2.1) such as:

1. Former grains of anhydrous silicates, now completely replaced, are present within a few hundred micrometers of minimally-altered-to-unaltered anhydrous silicate grains, even within Lithologies A and B (petrologic subtypes CM2.2 and 2.1, respectively (Suttle et al., 2022); Figures S1–S3); similar to textures described in other CMs (Bischoff et al., 2017; Metzler et al., 1992; Noguchi et al., 2021; Suttle et al., 2021; Zolensky et al., 1997).

2. Some surviving olivine fragments in the matrix only have serpentine veins on their interior, while their exterior in contact with hydrated matrix shows no reaction rim (Figure 7a,b,f–h). This texture is consistent with brecciation predominantly post-dating aqueous alteration.

3. Surviving fragmental grains of olivine in the matrix are, on average, less aqueously altered than chondrule olivines of similar size (Figure 7), similar to textures described by Jacquet et al. (2021).

However, other fine-grained matrix olivine grains in the same location may have been completely replaced (Figure 7, Figures S1–S3).

4. Cross-cutting relationships between phyllosilicate veins and primary olivine grains are truncated by fractures infilled by hydrated matrix, with no evidence for fluid driven alteration textures being observed in the olivine or olivine-hosted phyllosilicates in contact with the vein despite evidence for aqueous alteration of the olivine elsewhere in the same grain (Figure 7a,b).

5. Fayalitic olivine fragments, which should be more susceptible to alteration by fluids than forsteritic grains (Brearley, 2003, 2006; Hanowski & Brearley, 2001; Suttle et al., 2021), survive in lithologies where the forsteritic grains have been partially to completely replaced (Figure 7c–e);

6. There is a large geochemical variation in the composition of secondary phases in the matrix TCI-like object rims and FGRs that does not correlate with degree of alteration (Figures 3 and 4). This is consistent with other descriptions of CMs (McSween Jr, 1979a, 1987; Noguchi et al., 2021; Zolensky et al., 1993).

7. No geochemical correlation exists between the extent of aqueous alteration and the spread of chemistry of matrix, TCI—like object rims, FGRs, and secondary phases in chondrules and CAIs which overlap significantly (Figures 3 and 4).

8. Secondary mineral assemblages hosted within chondrules, CAIs, and anhydrous silicates are geochemically distinct relative to those in the matrix, TCI-like objects, and FGRs (Table 1, Figures 3 and 4, Figures S4 and S5).

9. The amorphous silicate with embedded sulfide and oxide objects we observed and other phases that are typically thought to be fluid susceptible are seen to survive relatively unaltered in FGRs within nanometers of phyllosilicates in lithologies of high (CM2.1–2.2) petrologic types in Winchcombe lithologies (Figure 9e,f).

10. Partial replacement of fluid susceptible metastable aragonite (Brown et al., 1962) with calcite and partial to complete replacement of carbonate assemblages with TCI-like objects (Figure 6c–f).

It should be noted that all these observations occur away from the clear lithological boundaries that separate lithologies A–H and Mx (King et al., 2022; Suttle et al., 2022) and so cannot be simply explained by macroscale brecciation (Bischoff et al., 2017; Lentfort et al., 2021).

Here we discuss the implications of these observations on the length scale of brecciation and heterogeneity of aqueous alteration extent of Winchcombe. We propose

that while many of the above observations can be explained by parent body-driven alteration, many of these observations provide evidence that some of the primary accretionary mineralogy may survive or can be inferred from the textures of the secondary phases, even in heavily aqueously altered CM lithologies, and that the CM parent body was disrupted and reaccreted at a granular level after the final episode of aqueous alteration.

## CM Aqueous Alteration

Given a sufficient water/rock ratio, times cale, permeability, and accessibility of fluid to reactive mineral surfaces, fluid-mediated alteration reactions that occur within a solid rock should equally affect reactive mineral grains within the rock, resulting in an equilibrium mineral assemblage (Fulignati, 2020; Velbel, 2014; Velbel et al., 2012). Winchcombe provides further evidence for parent body scale alteration. The similarity of TCI-like object core compositions between lithologies (Figure 4d) is consistent with production from the same fluid (Fulignati, 2020; Putnis & Austrheim, 2010). However, this uniform composition could also be explained by distinct fluids that altered the different lithologies but ultimately evolved to the same steady state equilibria (Velbel et al., 2012, 2015). Either way the formation of TCI-cores is likely the final stage of parent body aqueous alteration.

If any of these aforementioned factors are absent, then local disequilibrium mineral assemblages would form (Velbel et al., 2012, 2015). There is strong evidence that aqueous alteration of the CM meteorites to varying degrees occurred early on the parent body in the presence of an evolving heterogeneous localized fluid (Brearley, 2003; Hewins et al., 2014; Lee et al., 2012, 2014; Lindgren et al., 2017; Metzler et al., 1992; Rubin et al., 2007; Suttle et al., 2021), for example, centimeter-scale reaction fronts (Hanowski & Brearley, 2000; Jacquet et al., 2016), mineral veins that cut through matrix and chondrules (Lee et al., 2012; Lindgren et al., 2017) and element mobility between chondrule mesostasis and the chondrule/rim boundary limited to a few 10s of micrometers (Chizmadia & Brearley, 2004). In addition, there is evidence in the carbonate mineralogy for multiple generations of fluid (Lee et al., 2012, 2014).

Localized heterogeneity in aqueous alteration extent of components within individual clasts of CM chondrites could be reconciled by invoking one of or a combination of processes including:

1. Variations in porosity and permeability limiting access for fluids to the reactive surface (Bland et al., 2009; Hanna et al., 2022). This would produce microchemical environments with distinct fluids and short time scales of reaction that permit early formed phases to persist metastably (Hanowski & Brearley, 2001; Singerling & Brearley, 2020).
2. Heterogeneous accretion of ices or deriving water externally for alteration of CMs resulted in regions of variable water/rock ratios (Verdier-Paoletti et al., 2019) such that in regions with low water/rock ratios, the reactive fluid would be locally exhausted before all minerals are replaced (Howard et al., 2015; Velbel et al., 2012).
3. Replacement reactions isolating (e.g., "armoring") the reactive surface and preserving an anhydrous core (Montes-Hernandez et al., 2010; Putnis & Austrheim, 2010).
4. Evolution of fluid chemistry and/or pH or multiple generations of chemically distinct fluids that variably promote the dissolution and replacement of specific phases that change over time or very short duration aqueous alteration (Lee et al., 2012; Lindgren et al., 2017; Oelkers et al., 2018; Pignatelli et al., 2016).
5. Alteration of each component in a different location prior to the accumulation of the host rock (Bischoff, 1998; Metzler et al., 1992), comparable to the process in sedimentary rocks where aqueously altered minerals are deposited alongside other minerals that do not have a metasomatic history. This mechanism would require brecciation and abrasion of the CM meteorite components on a length scale shorter than that of individual lithologies.

## Geochemical Heterogeneity of Matrix TCI-Like Object Rims

The chemical heterogeneity of the matrix TCI-like object rims and secondary minerals (Figures 3 and 4) can be explained by one or multiple of the above processes working in isolation or in tandem, and is likely due to local variations in porosity and permeability. Numerical modeling has shown that the matrix of chondrites, although highly porous, is impermeable over distances >100 μm during the time scales associated with fluid alteration (Bland et al., 2009). The heterogeneous primary matrix of CMs and the heterogeneous distribution of chondrules and CAIs, being altered by these isolated fluids, would result in microchemical environments which would metastably preserve early formed secondary phases and produce highly heterogeneous secondary mineral assemblages (Hanowski & Brearley, 2001; Palmer & Lauretta, 2011; Rubin, 2012; Singerling & Brearley, 2020; Yang et al., 2022).

In addition, some of the heterogeneity in the matrix relative to previous CM studies could be due to using a focused electron beam used to collect the EDS data. This

smaller interaction volume of the electron beam would highlight more clearly local chemical and mineralogical heterogeneities in the matrix.

An excellent way to introduce heterogeneities in permeability into a rock is along petrofabrics and fractures (Rubin, 2012; Yang et al., 2022; Zhang, 2013). Data from μCT and SEM reveal that half of the Winchcombe chips studied exhibit a foliation fabric defined by the chondrule long shape axis. Similar foliation textures have been observed in other CM chondrites, (e.g., Hanna et al., 2015; Lindgren et al., 2015; Vacher et al., 2018), and other carbonaceous chondrite meteorites, (e.g., Charles et al., 2018; Tait et al., 2016). We interpret these petrofabrics as being formed by impact compaction, in line with previous studies (Hanna et al., 2015; Tomeoka et al., 1999; Vacher et al., 2018). Differences in the orientation of any foliation fabric between two lithologies within the same meteorite sample (Figure 1) indicate that the petrofabric-forming impacts must have occurred prior to the formation and final lithification of the ultimate Winchcombe breccia. In addition, the CM lithologies that exhibit a chondrule fabric also exhibit a shape preferred orientation fabric for the pores and grains in the matrix. However, this matrix fabric appears to be perpendicular to the chondrule fabric (Figures 2c and 5b), though only one region of matrix was investigated in this way. This difference in matrix and chondrule fabrics could be due to multiple impacts (Lindgren et al., 2015) or caused by heterogeneous response of matrix materials to compaction (Bland et al., 2014). Further work is needed to discern the cause of the difference in shape fabric orientations between chondrules and matrix.

Some Winchcombe samples also have fractures that align with this foliation (Figure 1a,c, and File S2). This relationship is consistent with fracture generation facilitated by a rock cleavage (Powell, 1979). Fluid modeling reveals that, at the macroscale, these fractures could act as highly permeable pathways (Table S1), in which case such fractures may facilitate fluid ingress and transport during parent body aqueous alteration (Lee et al., 2012). Anisotropic rocks are much more permeable in the plane of a foliation fabric than across the foliation (Zhang, 2013). However, there does not seem to be any evidence of increased aqueous alteration in association with these fractures or precipitation of minerals within them as has been reported for veins in CMs previously (Lee et al., 2012) (Figures S1–S3). Therefore, it is likely that although these fractures occur along the foliation fabric, they formed after aqueous alteration and potentially even as recently as the meteorite's fall to Earth. Thus, these fractures, foliations, and their associated permeability are likely to have had limited to no control on the pathways for fluids to reach reactive sites on the Winchcombe meteorite's parent body.

## Evolution and Provenance of TCI-Like Objects and Carbonates

TCI-like objects are a characteristic mineral assemblage of CMs and have been interpreted to form early from the aqueous alteration of Fe-Ni metal beads and anhydrous silicate grains (Pignatelli et al., 2017; Tomeoka & Buseck, 1985). Carbonates are also a key indicator for the extent of parent body aqueous alteration (Lee et al., 2012, 2014; Lee & Ellen, 2008). The homogeneous composition of TCI-like object cores across Winchcombe lithologies suggest it is likely that TCI-like objects and the carbonate assemblages sometimes found within them, formed early during aqueous alteration from the same fluid on the asteroid parent body (Fulignati, 2020). Similarly, carbonate assemblages have been interpreted as forming from multiple generations of fluids on the CM parent body (Lee et al., 2012, 2014; Lee & Ellen, 2008).

Aragonite is formed during the early stages of aqueous alteration and has only been reported in meteorites with low degrees of aqueous alteration (Lee et al., 2014; Rubin et al., 2007) but may still persist metastably to higher degrees of aqueous alteration. Dolomite and breunnerite only occur in those meteorites that exhibit higher degrees of aqueous alteration (Lee et al., 2014; Rubin et al., 2007). Calcite is found across a range of petrologic subtypes (Lee et al., 2014; Rubin et al., 2007). In petrologic types reflecting the high degrees of aqueous alteration, calcite, dolomite, and breunnerite are partially replaced by TCI-like objects (Fe-rich serpentine followed by Mg-rich serpentine) (Lee et al., 2012, 2014). Our observations of Winchcombe are broadly consistent with previous work but provide additional details.

Scanning electron microscopy (SEM) and EBSD investigations reveal that Winchcombe lithologies contain a variety of carbonate phases including aragonite (lithology A, subtype 2.2), calcite, and dolomite (lithology F, subtype 2.0; Figure 6, Figure S6). However, it was only possible to distinguish calcite and aragonite by a crystallographic analysis such as EBSD, Raman, or CL, which were only used for lithology A (subtype 2.2), and so aragonite may be more common in CM meteorites than currently thought especially as it has also been found in relatively low petrologic types (Lee et al., 2014; Lee & Ellen, 2008). The polymineralic calcium carbonate–phyllosilicate–dolomite grain (Figure S6b) from lithology F is unusual for CMs, although petrographically similar to the calcite–breunnerite–dolomite grains in the highly aqueously altered CM QUE 93005 (Lee et al., 2012). The texture of the carbonate grains in Figures S6a–c indicates that they must have formed in the sequence calcium carbonate, phyllosilicate, and dolomite. The lack of inclusions in the lithology A carbonate grains together

with the CL zoning and straight crystal facets of all carbonate assemblages that are parallel to a crystallographic axis and perpendicular to the edge of the assemblage is consistent with carbonate growth into fluid-filled pores (Figure 6c–e, Figure S6d–g) in common with type 1 calcite grains in many other CMs (Lee et al., 2014; Lee & Ellen, 2008; Suttle et al., 2022).

In one location in lithology A, aragonite is in contact with a calcite cluster (Figure 6c–e). The internal deformation and straight-to-curved mechanical twins observed within the aragonite in EBSD data sets are consistent with dislocation creep (Figure 6d,e). This suggests that the aragonite experienced a deformation event that we tentatively interpret as related to impact shock and these textures and interpretation are consistent with TEM microstructural measurements of shocked carbonates in other CM chondrites (Dobrică et al., 2022). Our EBSD data also show that adjacent calcite is undeformed, indicating that it did not experience the same deformation event as the aragonite (Figure 6e). Where aragonite and calcite are present within the same grain, a crystallographic orientation relationship between the two phases is observed, as evidenced by similar IPF colors, as well as very similar grain boundary morphologies consistent with epitaxial replacement of one phase by the other (Figure 6d). During solid state replacement reactions deformation microstructures are erased (Putnis et al., 2009). We thus propose that aragonite is being epitaxially replaced by calcite (Putnis et al., 2009). This is consistent with the previous studies of carbonates in CM chondrites that suggest that aragonite is an early formed phase during parent body alteration (Lee et al., 2014; Lee & Ellen, 2008). The deformation of aragonite and lack of deformation in calcite suggests that between episodes of alteration the Winchcombe parent body was deformed likely via impact induced shock. This impact may be the same one that produced the petrofabric.

Many TCI-like objects in Winchcombe exhibit textural similarities to carbonates. TCI-like objects in Winchcombe have subdomains bounded by an Fe-rich phase with straight boundaries perpendicular to the grain edge that meet at 120° triple junctions in the center of the TCI-like object (Figure 6f,g). These textures show a striking similarity to the morphology of carbonate assemblages (Figure 6c–e). In addition, the drusy textures of TCI-like objects suggest inward growth of hydrous phases nucleated on the margins of the region, with the Fe-rich phase growing first, followed by Mg-rich serpentine. The drusy textures form by the precipitation of crystals into a fluid filled space by nucleation on a substrate. Some TCI-like objects have central voids (Suttle et al., 2022) supporting the presence of fluid-filled cavities produced by the dissolution of a precursor phase. This implies that transient porosity generation occurs at a later stage in the aqueous alteration of CM chondrites producing pockets of fluid.

In many places, calcite is partially replaced by TCI-like objects (Figure 6f). Here the Fe-rich phase of the TCI-like object surrounds and penetrates the calcite (Figure 6f). The orientation of the Fe-rich phases is controlled by the orientation of the calcite crystal and penetrate along grain boundaries and mineral cleavage (Figure 6f). The textural similarity between some TCI-like objects and carbonates as well as evidence for the partial replacement of calcite assemblages by TCI-like objects (Figure 6) suggests that many TCI-like objects were formerly carbonate. Although many TCI-like objects also likely formed from the alteration of metal and anhydrous silicates (Pignatelli et al., 2017), the abundance of TCI-like objects with the identical microstructures to carbonates in some lithologies suggests that carbonates are an additional precursor phase.

Overall, the textures observed here imply a progressive alteration sequence whereby aragonite forms first growing into pore space, is deformed, and then epitaxially replaced by calcite. The calcite is in turn replaced by Fe-rich component of TCI-like objects. Replacement exploits grain boundaries and mineral cleavages followed by partial to complete dissolution of calcite and precipitation of Mg-rich serpentine during the final stages of aqueous alteration. In Winchcombe, all steps of this alteration pathway are preserved (Figure 6). The preservation of the entire alteration sequence has several implications. First, carbonates must also be a precursor phase to TCI-like objects alongside metal and anhydrous silicate (Pignatelli et al., 2017). Second, the frequency of carbonate-like microstructures in many TCI-like objects suggests that many were originally carbonate, therefore some lithologies in Winchcombe, and by extension many CM chondrites, may have originally been very carbonate-rich (15%–40%, Suttle et al., 2022). If carbonate abundance was indeed this high, a key question is where the carbonate came from and where it went, as most CMs, even those CMs with low degrees of aqueous alteration have much less C and Ca (1%–3%) (Kerridge, 1985; Vacher et al., 2020) than would be predicted if many TCIs have replaced carbonate. In addition, the bulk composition of CMs are remarkably similar despite aqueous alteration. A potential explanation for where the carbonate went could be provided by observations of Bennu by the OSIRIS-REx mission revealing large carbonate veins on the asteroids' surface (Kaplan et al., 2020). Similar bulk compositions could be explained if the carbonate forming and removal process affected CMs nearly uniformly, which is plausible given the ubiquity of TCI-like objects in CMs. Higher abundances of C could have been initially sourced from accreted C-rich ices (Alexander et al., 2015). Additionally,

TCI-like objects could also form from growth into voids or from replacement of metal and anhydrous silicates (Pignatelli et al., 2017; Suttle et al., 2021, 2022). Thus, although the initial carbonate component was likely higher than currently thought, the 15%–40% initial carbonate abundances should be considered an absolute maximum. However, some clasts in the CM LON94101 have 46 vol% carbonate (Lindgren et al., 2013) giving weight to the idea that some CMs, at least in localized regions, may initially have been very carbonate rich. Third, similar to the survival of anhydrous silicates discussed later, the observations that aragonite is being heterogeneously replaced by calcite, and that in turn calcite is being heterogeneously replaced by TCI-like objects, show the full dynamic range of alteration. This alteration range spans from unaltered carbonates to partially replaced carbonates with TCI-like objects to complete replacement of carbonates with TCI-like objects all within the same lithology. The preservation of the progress of the entire reaction suggests that the abundance of fluid was variable across the CM parent body and locally became exhausted in some locations, prior to reaction completion. This was then followed by brecciation and reaccretion of the CM parent body at a granular level emplacing objects with different alteration histories next to each other.

In particular, the survival of aragonite in lithology A (subtype 2.2) of the Winchcombe meteorite is puzzling in the framework of parent body aqueous alteration. Experiments show that, at low temperatures, the transformation from aragonite to calcite is 10 orders of magnitude faster in the presence of water than in the dry system (Brown et al., 1962; Putnis et al., 2009). Thus, aragonite replacement by calcite in the presence of a fluid should naturally reach completion—aragonite should not be observed in CMs. Aragonite–calcite does not require the presence of a fluid to mediate the phase change. If this phase change occurred under dry, cold conditions, then the replacement reaction may not have reached completion resulting in the survival of some aragonite, but critically this implies that aragonite was not exposed to water later in the alteration process for prolonged periods.

### Survival of Amorphous Silicates with Embedded Sulfides/Oxides and Partial Alteration of Organic Nanoglobules in Otherwise Hydrated FGRs

The nano-sulfide/oxide objects embedded in amorphous silicates that occur in P30552 (lithology A, subtype 2.2) FGRs resemble sub-micrometer-sized sulfide-rich regions of the FGRs of Yamato-791198 (Chizmadia & Brearley, 2008). This is a mildly aqueously altered CM. The sulfide-rich regions in Y791198 contain nanoscale Fe-Ni sulfides (<1 to ~200 nm size pentlandite/Ni-rich pyrrhotite) in amorphous/nanocrystalline silicate material,

which were interpreted as preserved nebular dust (Chizmadia & Brearley, 2008). The Winchcombe nano-sulfide/oxide objects also have petrographic similarities to the matrix in the least aqueously altered parts of the CM Paris that host sub-micrometer-sized amorphous silicate grains containing Fe-sulfide nanograins (Hewins et al., 2014; Leroux et al., 2015). This material was described as being GEMS-like (Leroux et al., 2015), with GEMS referring to glass with embedded metal and sulfide grains that have been described from anhydrous interplanetary dust particles (Bradley, 1994a, 1994b; Keller & Messenger, 2011). The nano-sulfide/oxide objects are not GEMS but do bear some petrographic and mineralogical similarities to the nano-sulfide bearing amorphous silicate in the mildly altered CMs Yamato-791198 and Paris and weakly altered CM Asuka-12659. More work on Winchcombe FGRs is needed in order to determine the mineralogy of the sulfide/oxide grains and determine the chemical composition, hydration, oxidation state, and crystallinity of the enclosing material.

Objects like the amorphous silicate with embedded nano-sulfides and or/oxides reported here are typically highly sensitive to fluid alteration and are quickly replaced (Leroux et al., 2015; Metzler et al., 1992). The survival of similar objects in other chondritic meteorites, beyond minor hydration and oxidation (Le Guillou et al., 2015), has been interpreted as evidence for limited aqueous alteration on their parent body (Leroux et al., 2015; Metzler et al., 1992), low temperature fluids that prevent recrystallization to phyllosilicates and therefore preserve the amorphous material as a metastable phase (Le Guillou et al., 2015; Le Guillou & Brearley, 2014), or brecciation and reaccreting of the FGR juxtaposing hydrated and anhydrous materials (Metzler et al., 1992; Noguchi et al., 2021). Here we observe such an amorphous silicate grain with embedded sulfide and oxides surviving with minor evidence that this object has been partially altered (very thin wisps of phyllosilicate within the grain; Figure 9f) within a FGR in lithology A (Figure 9d–f). Lithology A has been assigned a petrologic subtype CM2.2 (Suttle et al., 2022) indicating severe parent body aqueous alteration (Rubin et al., 2007) and so its presence is not due to limited parent body aqueous alteration (Leroux et al., 2015; Metzler et al., 1992). In addition, the amorphous silicate grain is within a few nm of hydrated phyllosilicates (Figure 9d–f), so its presence is not due to low fluid temperatures that inhibit phyllosilicate growth (Le Guillou et al., 2015; Le Guillou & Brearley, 2014).

The most likely explanation for the retainment of this amorphous silicate in this FGR with only minor alteration/hydration is that the FGR mineralogy was established prior to the FGRs accretion onto its present core object by brecciation, accretion, and juxtaposition of hydrated phyllosilicates and amorphous silicates, and after

the accretion of this inclusion and its FGR onto the asteroid, it was not subsequently subjected to aqueous alteration (Metzler et al., 1992; Noguchi et al., 2021). If the asteroid was altered post accretion of the FGR inclusion, this would either require low temperature fluids, or the reaction was chemically limited as before (Le Guillou et al., 2015; Le Guillou & Brearley, 2014), or that the amorphous silicate was isolated from pore fluid for all, or most, of the aqueous alteration. Isolation could occur through sealing of areas of the pore network by early secondary products, or encapsulation of grains within early formed cementing material. Indeed, encapsulation in early cements has been proposed in terrestrial sedimentary rocks for the survival of S-type cosmic spherules, which are sensitive to aqueous alteration (Suttle & Genge, 2017). Additionally, although the FGR is porous (Figure 9d), this does not necessarily equate to increased permeability (Bland et al., 2009) and therefore the amorphous silicate grain could be preserved intact through a minor aqueous alteration event which may have produced the fine wisps of phyllosilicate. Recent studies have suggested that amorphous silicates may be a carrier for water in the solar system and were accreted in a partially hydrated state from the nebular (Marrocchi et al., 2023).

The Winchcombe organic nanoglobules found in FGRs in lithology A (Subtype 2.2) are morphologically comparable to those that occur widely in different groups of primitive meteorites (De Gregorio et al., 2013; Garvie & Buseck, 2004). Some of the Winchcombe nanoglobules have been partially replaced by fine-grained phyllosilicate (Figure 9b,c), showing that they were formed before at least some of the aqueous alteration. Therefore these nanoglobules could have been accreted from interstellar environments (De Gregorio et al., 2013). This provides supporting evidence that suggest the FGR mineralogy was established from brecciation and juxtaposition of multiple components prior to accretion onto the asteroid (Metzler et al., 1992; Noguchi et al., 2021) and perhaps only experienced very minor aqueous alteration on the asteroid.

## Granular Scale Brecciation of CMs

If the FGR mineralogy was established prior to rim accretion and subsequent accretion of the FGR and the inclusion it is mantled around into the parent rock, and the FGR experienced little to no post accretion aqueous alteration post accretion, then it stands to reason that all other components found in Winchcombe lithologies including chondrules, chondrule fragments, and matrix were also emplaced then, and experienced brecciation and disaggregation at a granular level followed by reaccretion after the cessation of aqueous alteration (Bischoff et al., 2017; Hanna et al., 2015; Lentfort et al., 2021; Metzler et al., 1992; Rubin, 2012). The mechanism to produce

granular level disaggregation is likely impact-induced disruption of the CM parent body's surface to produce a regolith breccia similar to that proposed to produce the macroscale brecciation (Bischoff et al., 2017; Lentfort et al., 2021). Our observations of chondrule fabrics and heterogeneous deformation histories between carbonate generations suggest that CM lithologies were affected by multiple impacts that occurred during aqueous alteration (Lindgren et al., 2015). However, the disruption mechanism via impacts would have to be relatively gentle given the low shock state of the CM meteorite and lack of deformation microstructures observed in the calcite and olivine. This repeated disruption and reaccretion of the CM parent body would readily explain observations of variable alteration extents between similar juxtaposed materials, that is, unaltered olivine in close proximity to partially altered olivine or completely altered former olivine pseudomorphs and the survival of typically more fluid sensitive phases such as Fe-rich olivine (Bischoff, 1998; Brearley, 2003; Leroux et al., 2015; Metzler et al., 1992; Pinto et al., 2022; Zanetta et al., 2021, 2022). Serpentine veins hosted within anhydrous silicates, but not on their exterior (Figure 7), could also be explained by abrasion of the exterior of the grain after aqueous alteration which effectively removed the serpentine rim from the periphery. The lack of similar serpentine fragments in the matrix surrounding the grain suggests that the abrasion occurred prior to accretion of the grain, requiring brecciation (Bischoff et al., 2017; Lentfort et al., 2021; Metzler et al., 1992).

Thus, it likely that regolith gardening of the surface of the CM parent body over the same time period or after aqueous alteration could result in progressive cycles of aqueous alteration, disruption, reaccretion of fragments with different aqueous alteration histories and hydraulic fragmentation, that would explain the juxtaposition of anhydrous olivine next to hydrated matrix. However, as noted before the disruption events would have to be relatively gentle to avoid producing deformation microstructures in calcite and olivine. If this model is correct, then in the same way that Winchcombe is a breccia of eight CM lithologies (Suttle et al., 2022), each lithology within Winchcombe itself is formed from assembled components with different alteration histories. A breccia in a breccia, if you will. Lentfort et al. (2021) recently showed that CM breccia clasts do contain smaller clasts inside them, here we take this one step further and propose each individual grain could be considered its own discrete clast.

One challenge for this model is how can a lithified rock like a modern CM meteorite be disrupted at a granular level. However, there is growing evidence that CM meteorites may have initially been largely unlithified or only weakly lithified (Bland & Travis, 2017). This

includes observations of matrix infilling fractures in between chondrules and alignment of the matrix from compaction (Forman et al., 2017). In some locations in Winchcombe, we see similar features including fractures filled with matrix material that cut across both anhydrous silicates along with their phyllosilicate veins as well as TCI-like objects (Figures 6b and 7g,h). When associated with TCI-like objects, these matrix-filled fractures penetrate along grain boundaries evidenced by similar geometries and topologies of the TCI-like objects either side of the veins since their margins have matching topologies (Figure 6b). Crack terminations of matrix-filled fractures in TCI-like objects and anhydrous silicates suggest fracture growth by fluid-mediated crack-tip propagation. The observation of coarse serpentine group minerals within the center of these putative veins is consistent with formation by fluid. However, the presence of small tochilinite crystals and inclusions of matrix in this area, and the absence of any aqueous alteration reaction surfaces particularly within olivine in contact with matrix veins and despite evidence that those same olivine grains do exhibit evidence for aqueous alteration elsewhere on their surfaces or in veins suggests vein formation occurred after significant aqueous alteration of the matrix; after parent body alteration had ceased as olivine can start to react within days even at low temperatures in the presence of an aqueous fluid (Martin & Fyfe, 1970) or that the fluid that altered the matrix was more alkaline and inhibited the alteration of olivine (Wogelius & Walther, 1992). The presence of matrix in these veins is interesting as the fractures do not appear to penetrate back into the matrix and, as such, must have been formed while the matrix was unlithified, but in the absence of an aqueous fluid to avoid altering the olivine (Martin & Fyfe, 1970) or at least absence of a fluid of the correct pH or chemistry that would affect olivine (Hanowski & Brearley, 2001; Wogelius & Walther, 1992). An unlithified, but dry, matrix would allow it to flow into the crack, as well as preventing alteration of newly exposed olivine surfaces (Figure 7a,b). Similar flow features have been described in Allende and other CMs (Bischoff et al., 2017; Forman et al., 2017). These matrix-filled cracks in Winchcombe are, therefore, additional evidence that matrix can be mobilized, at least over a few hundred micrometers, as a slurry in which mineral particulates are fluidized. Hydraulic fragmentation implies elevated fluid pressures, which might be transient and caused by shock combined with the formation of impermeable barriers to fluid flow that result in the accumulation of pore-fluids. Then to produce the coarser breccia texture of large discrete clasts present in CMs (Bischoff et al., 2017; Lentfort et al., 2021), the CM meteorite would ultimately have to become fully lithified to preserve coherent aggregate clasts. Evidence that the matrix of the Winchcombe meteorite was, at some point

and at least locally, unlithified suggests that preserving isochemical reaction signatures in CM meteorites could be reconciled via a convecting mud slurry (Bland & Travis, 2017). In addition, CMs being unlithified for some of their history would make it very easy to disrupt and reaccrete CM material at a granular level juxtaposing fragments with different alteration histories. Some CMs that preserve primary accretionary textures must not have been affected by disruption post alteration. As such, we propose that each individual component in CM breccias should be considered its own discrete clast with its own alteration history that is likely separate from the materials it is currently in contact with.

**Implications for CM Classification**

Several classification systems have been proposed to assess the severity of the action of water on the CM asteroid (Alexander et al., 2013; Rubin et al., 2007; Suttle et al., 2021). The Rubin et al. (2007) scale of CM3.0 (unaltered) to CM2.0 (completely altered) is caused by heterogeneous accretion of ices in different regions of the CM parent asteroid providing variable water rock ratios that can consume and replace more or less of the primary mineralogy (Alexander et al., 2018; Brearley, 2006; Kimura et al., 2020; Rubin et al., 2007; Verdier-Paoletti et al., 2019). Similarly, macroscale brecciation is important to consider when classifying CM chondrites aqueous alteration extent to identify lithological boundaries and consider each clast separately (Bischoff et al., 2017; Lentfort et al., 2021). The evidence for granular level brecciation and reaccretion of at least the CM breccias presented here means care should be taken when classifying and interpreting the CM aqueous alteration extent within clasts because, if many CMs experienced this process, then it is likely that some unaltered or partially altered anhydrous fragments could be introduced into an otherwise full altered lithology from less altered regions of the CM parent body.

## CONCLUSIONS

Coordinated microanalysis from cm-atom scales across multiple sections of the Winchcombe meteorite has permitted detailed observations of the micro-texture of this CM chondrite breccia. The observations of the heterogeneous distribution of aqueous alteration assemblages, cross-cutting relationships and disequilibrium mineral assemblages have several key implications for the formation and evolution of the CM parent body(ies) and how we assess aqueous alteration of meteorites.

1. It is plausible to explain most of the heterogeneity in the nature and intensity of aqueous alteration

replacement reactions by localized variations in permeability, water/rock ratios, temperature, fluid chemistry and pH, consumption of fluids, and isolation/armoring of reactive surfaces consistent with the established literature.

2. The secondary mineral assemblage retains textural signatures of the precursor phases which could permit the original mineralogy of CM meteorites to be reconstructed. Phase heritage from TCI-like objects suggests that carbonates may have been a greater component of CMs during early aqueous alteration than currently thought.

3. Not all aqueous alteration occurred in situ within each Winchcombe lithology. Disruption, abrasion, and reaccretion of the CM parent body at a granular level and the clast level after aqueous alteration ceased (at least locally) may be required to juxtapose hydrated minerals next to traditionally water-sensitive phases at the micrometer to nanometer scale.

4. Granular level disruption of CMs could introduce grains of unaltered material into lithologies that are highly aqueously altered and vice-versa which could influence the petrologic subtype classification of CMs.

*Editorial Handling*—Dr. Adrian John Brearley

## REFERENCES

Alexander, C. M. O'D., Bowden, R., Fogel, M., and Howard, K. 2015. Carbonate Abundances and Isotopic Compositions in Chondrites. *Meteoritics & Planetary Science* 50: 810–833.

Alexander, C. M. O'D., Bowden, R., Fogel, M., Howard, K., Herd, C., and Nittler, L. 2012. The Provenances of Asteroids, and their Contributions to the Volatile Inventories of the Terrestrial Planets. *Science* 337: 721–23.

Alexander, C. M. O'D., Howard, K. T., Bowden, R., and Fogel, M. L. 2013. The Classification of CM and CR Chondrites Using Bulk H, C and N Abundances and Isotopic Compositions. *Geochimica et Cosmochimica Acta* 123: 244–260.

Alexander, C. M. O'D., McKeegan, K. D., and Altwegg, K. 2018. Water Reservoirs in Small Planetary Bodies: Meteorites, Asteroids, and Comets. *Space Science Reviews* 214: 1–47.

Andreani, M., Daniel, I., and Pollet-Villard, M. 2013. Aluminum Speeds up the Hydrothermal Alteration of Olivine. *American Mineralogist* 98: 1738–44.

Barber, D. 1981. Matrix Phyllosilicates and Associated Minerals in C2M Carbonaceous Chondrites. *Geochimica et Cosmochimica Acta* 45: 945–970.

Bischoff, A. 1998. Aqueous Alteration of Carbonaceous Chondrites: Evidence for Preaccretionary Alteration—A Review. *Meteoritics & Planetary Science* 33: 1113–22.

Bischoff, A., Ebert, S., Metzler, K., and Lentfort, S. 2017. *Breccia Classification of CM Chondrites.* Paper Presented at the 80th Annual Meeting of the Meteoritical Society, 6089.

Bland, P. A., Collins, G., Davison, T., Abreu, N., Ciesla, F., Muxworthy, A., and Moore, J. 2014. Pressure–Temperature Evolution of Primordial Solar System Solids during Impact-Induced Compaction. *Nature Communications* 5: 1–13.

Bland, P. A., Jackson, M. D., Coker, R. F., Cohen, B. A., Webber, J. B. W., Lee, M. R., Duffy, C. M., et al. 2009. Why Aqueous Alteration in Asteroids Was Isochemical: High Porosity≠ High Permeability. *Earth and Planetary Science Letters* 287: 559–568.

Bland, P. A., Stadermann, F. J., Floss, C., Rost, D., Vicenzi, E. P., Kearsley, A. T., and Benedix, G. K. 2007. A

Cornucopia of Presolar and Early Solar System Materials at the Micrometer Size Range in Primitive Chondrite Matrix. *Meteoritics & Planetary Science* 42: 1417–27.

Bland, P. A., and Travis, B. J. 2017. Giant Convecting Mud Balls of the Early Solar System. *Science Advances* 3: e1602514.

Bradley, J. P. 1994a. Chemically Anomalous, Preaccretionally Irradiated Grains in Interplanetary Dust from Comets. *Science* 265: 925–29.

Bradley, J. P. 1994b. Nanometer-Scale Mineralogy and Petrography of Fine-Grained Aggregates in Anhydrous Interplanetary Dust Particles. *Geochimica et Cosmochimica Acta* 58: 2123–34.

Brearley, A. J. 1995. Aqueous Alteration and Brecciation in Bells, an Unusual, Saponite-Bearing, CM chondrite. *Geochimica et Cosmochimica Acta* 59: 2291–2317.

Brearley, A. J. 2003. Nebular Versus Parent-Body Processing. *Treatise on Geochemistry* 1: 711.

Brearley, A. J. 2006. The Action of Water. *Meteorites and the Early Solar System II* 943: 587–624.

Brearley, A. J. 2021. Nanophase Iron Carbides in Fine-Grained Rims in CM2 Carbonaceous Chondrites: Formation of Organic Material by Fischer–Tropsch Catalysis in the Solar Nebula. *Meteoritics & Planetary Science* 56: 108–126.

Brown, W., Fyfe, W., and Turner, F. 1962. Aragonite in California Glaucophane Schists, and the Kinetics of the Aragonite—Calcite Transformation. *Journal of Petrology* 3: 566–582.

Bunch, T., and Chang, S. 1980. Carbonaceous Chondrites—II. Carbonaceous Chondrite Phyllosilicates and Light Element Geochemistry as Indicators of Parent Body Processes and Surface Conditions. *Geochimica et Cosmochimica Acta* 44: 1543–77.

Charles, C. R., Robin, P. Y. F., Davis, D. W., and McCausland, P. J. 2018. Shapes of Chondrules Determined from the Petrofabric of the CR 2 Chondrite NWA 801. *Meteoritics & Planetary Science* 53: 935–951.

Chizmadia, L. J., and Brearley, A. 2004. Formation of Fe-Enrichment Boundary Zones between Chondrules and their Fine-Grained Rims in the CM2 Chondrite, Y-791198. *Meteoritics and Planetary Science Supplement* 39: 5216.

Chizmadia, L. J., and Brearley, A. J. 2008. Mineralogy, Aqueous Alteration, and Primitive Textural Characteristics of Fine-Grained Rims in the Y-791198 CM2 Carbonaceous Chondrite: TEM Observations and Comparison to ALHA81002. *Geochimica et Cosmochimica Acta* 72: 602–625.

Clayton, R. N., and Mayeda, T. K. 1999. Oxygen Isotope Studies of Carbonaceous Chondrites. *Geochimica et Cosmochimica Acta* 63: 2089–2104.

Daly, L., Lee, M., Bagot, P., Halpin, J., Smith, W., McFadzean, S., O'Brien, A. C., Griffin, S., Hallis, L. J., and Cohen, B. 2020. Exploring Mars at the Nanoscale: Applications of Transmission Electron Microscopy and Atom Probe Tomography in Planetary Exploration. *IOP Conference Series: Materials Science and Engineering* 891: 012008.

Daly, L., Lee, M. R., Darling, J. R., McCarrol, I., Yang, L., Cairney, J., Forman, L. V., et al. 2021. Developing Atom Probe Tomography of Phyllosilicates in Preparation for Extra-Terrestrial Sample Return. *Geostandards and Geoanalytical Research* 45: 427–441.

Davidson, J., Alexander, C. M. O'D., Stroud, R. M., Busemann, H., and Nittler, L. R. 2019. Mineralogy and

Petrology of Dominion Range 08006: A Very Primitive CO3 Carbonaceous Chondrite. *Geochimica et Cosmochimica Acta* 265: 259–278.

Davidson, J., Busemann, H., Nittler, L. R., Alexander, C. M. O'D., Orthous-Daunay, F.-R., Franchi, I. A., and Hoppe, P. 2014. Abundances of Presolar Silicon Carbide Grains in Primitive Meteorites Determined by NanoSIMS. *Geochimica et Cosmochimica Acta* 139: 248–266.

De Gregorio, B. T., Stroud, R. M., Nittler, L. R., Alexander, C. M. O'D., Bassim, N. D., Cody, G. D., Kilcoyne, A. L. D., et al. 2013. Isotopic and Chemical Variation of Organic Nanoglobules in Primitive Meteorites. *Meteoritics & Planetary Science* 48: 904–928.

Dobrică, E., McCain, K. A., McKeegan, K. D., and Brearley, A. J. 2022. TEM Analyses of Carbonates from CM Chondrites-Possible Impact Events Revealed by Pervasive Microstructural Features. *Microscopy and Microanalysis* 28(S1): 2666–68.

DuFresne, E. R., and Anders, E. 1962. On the Chemical Evolution of the Carbonaceous Chondrites. *Geochimica et Cosmochimica Acta* 26: 1085–1114.

Forman, L., Bland, P., Timms, N. E., Daly, L., Benedix, G., Trimby, P., Collins, G. S., and Davison, T. M. 2017. Defining the Mechanism for Compaction of the CV Chondrite Parent Body. *Geology* 45: 559–562.

Fuchs, L. H., Olsen, E., and Jensen, K. J. 1973. Mineralogy, Mineral-Chemistry, and Composition of the Murchison (C2) Meteorite. *Smithsonian Contributions to the Earth Sciences* 10: 1–39.

Fulignati, P. 2020. Clay Minerals in Hydrothermal Systems. *Minerals* 10: 919.

Garvie, L. A., and Buseck, P. R. 2004. Nanosized Carbon-Rich Grains in Carbonaceous Chondrite Meteorites. *Earth and Planetary Science Letters* 224: 431–39.

Hamilton, V. E., Kaplan, H. H., Connolly, H. C., Jr., Goodrich, C. A., Abreu, N. M., and Simon, A. A. 2022. GRO 95577 (CR1) as a Mineralogical Analogue for Asteroid (101955) Bennu. *Icarus* 383: 115054.

Hanna, R. D., Ketcham, R. A., Edey, D. R., and O'Connell, J. 2022. 3D Porosity Structure of the Earliest Solar System Material. *Scientific Reports* 12: 1–8.

Hanna, R. D., Ketcham, R. A., Zolensky, M., and Behr, W. M. 2015. Impact-Induced Brittle Deformation, Porosity Loss, and Aqueous Alteration in the Murchison CM Chondrite. *Geochimica et Cosmochimica Acta* 171: 256–282.

Hanowski, N. P., and Brearley, A. J. 2000. Iron-Rich Aureoles in the CM Carbonaceous Chondrites Murray, Murchison, and Allan Hills 81002: Evidence for In Situ Aqueous Alteration. *Meteoritics & Planetary Science* 35: 1291–1308.

Hanowski, N. P., and Brearley, A. J. 2001. Aqueous Alteration of Chondrules in the CM Carbonaceous Chondrite, Allan Hills 81002: Implications for Parent Body Alteration. *Geochimica et Cosmochimica Acta* 65: 495–518.

Hewins, R. H., Bourot-Denise, M., Zanda, B., Leroux, H., Barrat, J.-A., Humayun, M., Göpel, C., et al. 2014. The Paris Meteorite, the Least Altered CM Chondrite So Far. *Geochimica et Cosmochimica Acta* 124: 190–222.

Hicks, L. J., Bridges, J. C., and Gurman, S. 2014. Ferric Saponite and Serpentine in the Nakhlite Martian Meteorites. *Geochimica et Cosmochimica Acta* 136: 194–210.

Howard, K., Alexander, C. M. O'D., Schrader, D. L., and Dyl, K. 2015. Classification of Hydrous Meteorites (CR,

CM and C2 Ungrouped) by Phyllosilicate Fraction: PSD-XRD Modal Mineralogy and Planetesimal Environments. *Geochimica et Cosmochimica Acta* 149: 206–222.

Jacquet, E., Barrat, J. A., Beck, P., Caste, F., Gattacceca, J., Sonzogni, C., and Gounelle, M. 2016. Northwest Africa 5958: A Weakly Altered CM-Related Ungrouped Chondrite, Not a CI 3. *Meteoritics & Planetary Science* 51: 851–869.

Jacquet, E., Piralla, M., Kersaho, P., and Marrocchi, Y. 2021. Origin of Isolated Olivine Grains in Carbonaceous Chondrites. *Meteoritics & Planetary Science* 56: 13–33.

Jarosewich, E. 1990. Chemical Analyses of Meteorites: A Compilation of Stony and Iron Meteorite Analyses. *Meteoritics* 25: 323–337.

Jenkins, L., Lee, M. R., Daly, L., King, A., Floyd, C., Martin, P.-E., Almeida, N. V., and Genge, M. 2022. Winchcombe: An Example of Rapid Terrestrial Alteration of a CM Chondrite. *Meteoritics & Planetary Science*.

Jones, C. L., and Brearley, A. J. 2006. Experimental Aqueous Alteration of the Allende Meteorite under Oxidizing Conditions: Constraints on Asteroidal Alteration. *Geochimica et Cosmochimica Acta* 70: 1040–58.

Kaplan, H., Lauretta, D., Simon, A., Hamilton, V., DellaGiustina, D., Golish, D., Reuter, D. C., et al. 2020. Bright Carbonate Veins on Asteroid (101955) Bennu: Implications for Aqueous Alteration History. *Science* 370: eabc3557.

Keller, L. P., and Messenger, S. 2011. On the Origins of GEMS Grains. *Geochimica et Cosmochimica Acta* 75: 5336–65.

Kerridge, J. F. 1985. Carbon, Hydrogen and Nitrogen in Carbonaceous Chondrites: Abundances and Isotopic Compositions in Bulk Samples. *Geochimica et Cosmochimica Acta* 49: 1707–14.

Kerridge, J. F., Mackay, A. L., and Boynton, W. V. 1979. Magnetite in CI Carbonaceous Meteorites: Origin by Aqueous Activity on a Planetesimal Surface. *Science* 205: 395–97.

Kimura, M., Imae, N., Komatsu, M., Barrat, J., Greenwood, R., Yamaguchi, A., and Noguchi, T. 2020. The most Primitive CM Chondrites, Asuka 12085, 12169, and 12236, of Subtypes 3.0–2.8: Their Characteristic Features and Classification. *Polar Science* 26: 100565.

King, A., Daly, L., Rowe, J., Joy, K. H., Greenwood, R. C., Devillepoix, H. A., Suttle, M. D., et al. 2022. The Winchcombe Meteorite, a Unique and Pristine Witness from the Outer Solar System. *Science Advances* 8: eabq3925.

Lafay, R., Montes-Hernandez, G., Janots, E., Chiriac, R., Findling, N., and Toche, F. 2012. Mineral Replacement Rate of Olivine by Chrysotile and Brucite under High Alkaline Conditions. *Journal of Crystal Growth* 347: 62–72.

Lamadrid, H. M., Rimstidt, J. D., Schwarzenbach, E. M., Klein, F., Ulrich, S., Dolocan, A., and Bodnar, R. J. 2017. Effect of Water Activity on Rates of Serpentinization of Olivine. *Nature Communications* 8: 1–9.

Lamadrid, H. M., Zajacz, Z., Klein, F., and Bodnar, R. 2021. Synthetic Fluid Inclusions XXIII. Effect of Temperature and Fluid Composition on Rates of Serpentinization of Olivine. *Geochimica et Cosmochimica Acta* 292: 285–308.

Lauretta, D. S., Hua, X., and Buseck, P. R. 2000. Mineralogy of Fine-Grained Rims in the ALH 81002 CM Chondrite. *Geochimica et Cosmochimica Acta* 64: 3263–73.

Le Guillou, C., and Brearley, A. 2014. Relationships between Organics, Water and Early Stages of Aqueous Alteration

in the Pristine CR3. 0 Chondrite MET 00426. *Geochimica et Cosmochimica Acta* 131: 344–367.

Le Guillou, C., Changela, H. G., and Brearley, A. J. 2015. Widespread Oxidized and Hydrated Amorphous Silicates in CR Chondrites Matrices: Implications for Alteration Conditions and H2 Degassing of Asteroids. *Earth and Planetary Science Letters* 420: 162–173.

Lee, M. R., Bland, P., and Graham, G. 2003. Preparation of TEM Samples by Focused Ion Beam (FIB) Techniques: Applications to the Study of Clays and Phyllosilicates in Meteorites. *Mineralogical Magazine* 67: 581–592.

Lee, M. R., Cohen, B. E., King, A. J., and Greenwood, R. C. 2019. The Diversity of CM Carbonaceous Chondrite Parent Bodies Explored Using Lewis Cliff 85311. *Geochimica et Cosmochimica Acta* 264: 224–244.

Lee, M. R., and Ellen, R. 2008. Aragonite in the Murray (CM2) Carbonaceous Chondrite: Implications for Parent Body Compaction and Aqueous Alteration. *Meteoritics & Planetary Science* 43: 1219–31.

Lee, M. R., Floyd, C., Martin, P. E., Zhao, X., Franchi, I. A., Jenkins, L., and Griffin, S. 2023. Extended Time Scales of Carbonaceous Chondrite Aqueous Alteration Evidenced by a Xenolith in L a P Az Icefield 02239 (CM2). *Meteoritics & Planetary Science* 58: 672–687.

Lee, M. R., Hallis, L. J., Daly, L., and Boyce, A. J. 2023. The Water Content of CM Carbonaceous Chondrite Falls and Finds, and their Susceptibility to Terrestrial Contamination. *Meteoritics & Planetary Science* 58: 1760–72.

Lee, M. R., Lindgren, P., and Sofe, M. R. 2014. Aragonite, Breunnerite, Calcite and Dolomite in the CM Carbonaceous Chondrites: High Fidelity Recorders of Progressive Parent Body Aqueous Alteration. *Geochimica et Cosmochimica Acta* 144: 126–156.

Lee, M. R., Lindgren, P., Sofe, M. R., Alexander, C. M. O'D., and Wang, J. 2012. Extended Chronologies of Aqueous Alteration in the CM2 Carbonaceous Chondrites: Evidence from Carbonates in Queen Alexandra Range 93005. *Geochimica et Cosmochimica Acta* 92: 148–169.

Lentfort, S., Bischoff, A., Ebert, S., and Patzek, M. 2021. Classification of CM Chondrite Breccias—Implications for the Evaluation of Samples from the OSIRIS-REx and Hayabusa 2 Missions. *Meteoritics & Planetary Science* 56: 127–147.

Leroux, H., Cuvillier, P., Zanda, B., and Hewins, R. H. 2015. GEMS-Like Material in the Matrix of the Paris Meteorite and the Early Stages of Alteration of CM Chondrites. *Geochimica et Cosmochimica Acta* 170: 247–265.

Lindgren, P., Hanna, R. D., Dobson, K. J., Tomkinson, T., and Lee, M. R. 2015. The Paradox between Low Shock-Stage and Evidence for Compaction in CM Carbonaceous Chondrites Explained by Multiple Low-Intensity Impacts. *Geochimica et Cosmochimica Acta* 148: 159–178.

Lindgren, P., Lee, M., Starkey, N., and Franchi, I. 2017. Fluid Evolution in CM Carbonaceous Chondrites Tracked through the Oxygen Isotopic Compositions of Carbonates. *Geochimica et Cosmochimica Acta* 204: 240–251.

Lindgren, P., Lee, M. R., Sofe, M. R., and Zolensky, M. E. 2013. Clasts in the CM 2 Carbonaceous Chondrite Lonewolf Nunataks 94101: Evidence for Aqueous Alteration Prior to Complex Mixing. *Meteoritics & Planetary Science* 48: 1074–90.

Mackinnon, I. D. 1980. *Structures and Textures of the Murchison and Mighei Carbonaceous Chondrite Matrices.* Paper Presented at the 11th Lunar and Planetary Science

Conference, Houston, TX, March 17–21, 1980, Volume 2 (A82-22296 09-91). New York: Pergamon Press, 839-852.

Marrocchi, Y., Bekaert, D. V., and Piani, L. 2018. Origin and Abundance of Water in Carbonaceous Asteroids. *Earth and Planetary Science Letters* 482: 23–32.

Marrocchi, Y., Gounelle, M., Blanchard, I., Caste, F., and Kearsley, A. T. 2014. The Paris CM Chondrite: Secondary Minerals and Asteroidal Processing. *Meteoritics & Planetary Science* 49: 1232–49.

Marrocchi, Y., Rigaudier, T., Piralla, M., and Piani, L. 2023. Hydrogen Isotopic Evidence for Nebular Pre-Hydration and the Limited Role of Parent-Body Processes in CM Chondrites. *Earth and Planetary Science Letters* 611: 118151.

Martin, B., and Fyfe, W. 1970. Some Experimental and Theoretical Observations on the Kinetics of Hydration Reactions with Particular Reference to Serpentinization. *Chemical Geology* 6: 185–202.

Matsumoto, M., Tsuchiyama, A., Nakato, A., Matsuno, J., Miyake, A., Kataoka, A., Ito, M., et al. 2019. Discovery of Fossil Asteroidal Ice in Primitive Meteorite Acfer 094. *Science Advances* 5: eaax5078.

McSween, H. Y., Jr. 1979a. Alteration in CM Carbonaceous Chondrites Inferred from Modal and Chemical Variations in Matrix. *Geochimica et Cosmochimica Acta* 43: 1761–70.

McSween, H. Y., Jr. 1979b. Are Carbonaceous Chondrites Primitive or Processed? A Review. *Reviews of Geophysics* 17: 1059–78.

McSween, H. Y., Jr. 1987. Aqueous Alteration in Carbonaceous Chondrites: Mass Balance Constraints on Matrix Mineralogy. *Geochimica et Cosmochimica Acta* 51: 2469–77.

McSween, H. Y., Jr., and Richardson, S. M. 1977. The Composition of Carbonaceous Chondrite Matrix. *Geochimica et Cosmochimica Acta* 41: 1145–61.

Metzler, K., Bischoff, A., and Stöffler, D. 1992. Accretionary Dust Mantles in CM Chondrites: Evidence for Solar Nebula Processes. *Geochimica et Cosmochimica Acta* 56: 2873–97.

Montes-Hernandez, G., Pommerol, A., Renard, F., Beck, P., Quirico, E., and Brissaud, O. 2010. In Situ Kinetic Measurements of Gas–Solid Carbonation of Ca (OH) 2 by Using an Infrared Microscope Coupled to a Reaction Cell. *Chemical Engineering Journal* 161: 250–56.

Nakamura-Messenger, K., Clemett, S. J., Messenger, S., and Keller, L. P. 2011. Experimental Aqueous Alteration of Cometary Dust. *Meteoritics & Planetary Science* 46: 843–856.

Noguchi, T., Yabuta, H., Itoh, S., Sakamoto, N., Mitsunari, T., Okubo, A., Okazaki, R., et al. 2017. Variation of Mineralogy and Organic Material during the Early Stages of Aqueous Activity Recorded in Antarctic Micrometeorites. *Geochimica et Cosmochimica Acta* 208: 119–144.

Noguchi, T., Yasutake, M., Tsuchiyama, A., Miyake, A., Kimura, M., Yamaguchi, A., Imae, N., Uesugi, K., and Takeuchi, A. 2021. Mineralogy of Fine-Grained Matrix, Fine-Grained Rim, Chondrule Rim, and Altered Mesostasis of a Chondrule in Asuka 12169, One of the least Altered CM Chondrites. *Polar Science* 29: 100727.

Oelkers, E. H., Declercq, J., Saldi, G. D., Gislason, S. R., and Schott, J. 2018. Olivine Dissolution Rates: A Critical Review. *Chemical Geology* 500: 1–19.

Ohtaki, K. K., Ishii, H. A., Bradley, J. P., Villalon, K. L., Davis, A. M., Stephan, T., Bustillo, K. C., and Ciston, J.

2021. Search for Meteoritic GEMS I: Comparison of Amorphous Silicates in Paris and Acfer 094 Chondrite Matrices and in Anhydrous Chondritic Interplanetary Dust Particles. *Geochimica et Cosmochimica Acta* 310: 320–345.

Palmer, E. E., and Lauretta, D. S. 2011. Aqueous Alteration of Kamacite in CM Chondrites. *Meteoritics & Planetary Science* 46: 1587–1607.

Pignatelli, I., Marrocchi, Y., Mugnaioli, E., Bourdelle, F., and Gounelle, M. 2017. Mineralogical, Crystallographic and Redox Features of the Earliest Stages of Fluid Alteration in CM Chondrites. *Geochimica et Cosmochimica Acta* 209: 106–122.

Pignatelli, I., Marrocchi, Y., Vacher, L. G., Delon, R., and Gounelle, M. 2016. Multiple Precursors of Secondary Mineralogical Assemblages in CM Chondrites. *Meteoritics & Planetary Science* 51: 785–805.

Pinto, G. A., Marrocchi, Y., Jacquet, E., and Olivares, F. 2022. Formation of Chondrule Fine-Grained Rims from Local Nebular Reservoirs. *Meteoritics & Planetary Science* 57: 1004–17.

Pirajno, F. 2012. *Hydrothermal Mineral Deposits: Principles and Fundamental Concepts for the Exploration Geologist.* Berlin: Springer Science & Business Media.

Powell, C. M. 1979. A Morphological Classification of Rock Cleavage. *Tectonophysics* 58: 21–34.

Putnis, A., and Austrheim, H. 2010. Fluid-Induced Processes: Metasomatism and Metamorphism. *Geofluids* 10: 254–269.

Putnis, A., Oelkers, E., and Schott, J. 2009. Mineral Replacement Reactions. *Thermodynamics and Kinetics of Water-Rock Interaction* 70: 87–124.

Rubin, A. E. 2012. Collisional Facilitation of Aqueous Alteration of CM and CV Carbonaceous Chondrites. *Geochimica et Cosmochimica Acta* 90: 181–194.

Rubin, A. E. 2015. An American on Paris: Extent of Aqueous Alteration of a CM Chondrite and the Petrography of its Refractory and Amoeboid Olivine Inclusions. *Meteoritics & Planetary Science* 50: 1595–1612.

Rubin, A. E., Trigo-Rodríguez, J. M., Huber, H., and Wasson, J. T. 2007. Progressive Aqueous Alteration of CM Carbonaceous Chondrites. *Geochimica et Cosmochimica Acta* 71: 2361–82.

Russell, S., King, A., Bates, H., Almeida, N., Greenwood, R., Daly, L., Joy, K. H., et al. 2022. Recovery and Curation of the Winchcombe (CM2) Meteorite. *Meteoritics & Planetary Science*.

Schmitt-Kopplin, P., Gabelica, Z., Gougeon, R. D., Fekete, A., Kanawati, B., Harir, M., Gebefuegi, I., Eckel, G., and Hertkorn, N. 2010. High Molecular Diversity of Extraterrestrial Organic Matter in Murchison Meteorite Revealed 40 Years after its Fall. *Proceedings of the National Academy of Sciences of the United States of America* 107: 2763–68.

Singerling, S., and Brearley, A. 2020. Altered Primary Iron Sulfides in CM 2 and CR 2 Carbonaceous Chondrites: Insights into Parent Body Processes. *Meteoritics & Planetary Science* 55: 496–523.

Suttle, M., Daly, L., Jones, R., Jenkins, L., Van Ginneken, M., Mitchell, J., Bridges, J. C., et al. 2022. The Winchcombe Meteorite—A Regolith Breccia from a Rubble-Pile CM Chondrite Asteroid. *Meteoritics & Planetary Science, Winchcombe Special Issue.*

Suttle, M., Folco, L., Genge, M., and Russell, S. 2020. Flying Too Close to the Sun–The Viability of Perihelion-Induced

Aqueous Alteration on Periodic Comets. *Icarus* 351: 113956.

Suttle, M., and Genge, M. J. 2017. Diagenetically Altered Fossil Micrometeorites Suggest Cosmic Dust Is Common in the Geological Record. *Earth and Planetary Science Letters* 476: 132–142.

Suttle, M., King, A., Schofield, P., Bates, H., and Russell, S. 2021. The Aqueous Alteration of CM Chondrites, a Review. *Geochimica et Cosmochimica Acta* 299: 219–256.

Tait, A. W., Fisher, K. R., Srinivasan, P., and Simon, J. I. 2016. Evidence for Impact Induced Pressure Gradients on the Allende CV3 Parent Body: Consequences for Fluid and Volatile Transport. *Earth and Planetary Science Letters* 454: 213–224.

Tomeoka, K., and Buseck, P. R. 1985. Indicators of Aqueous Alteration in CM Carbonaceous Chondrites: Microtextures of a Layered Mineral Containing Fe, S, O and Ni. *Geochimica et Cosmochimica Acta* 49: 2149–63.

Tomeoka, K., and Buseck, P. R. 1988. Matrix Mineralogy of the Orgueil CI Carbonaceous Chondrite. *Geochimica et Cosmochimica Acta* 52: 1627–40.

Tomeoka, K., McSween Jr, H. Y., and Buseck, P. R. 1989. Mineralogical Alteration of CM Carbonaceous Chondrites: A Review. *Paper presented at the Proceedings of the NIPR Symposium Antarctic Meteorites* 2: 221–234.

Tomeoka, K., Yamahana, Y., and Sekine, T. 1999. Experimental Shock Metamorphism of the Murchison CM Carbonaceous Chondrite. *Geochimica et Cosmochimica Acta* 63: 3683–3703.

Vacher, L. G., Marrocchi, Y., Villeneuve, J., Verdier-Paoletti, M. J., and Gounelle, M. 2018. Collisional and Alteration History of the CM Parent Body. *Geochimica et Cosmochimica Acta* 239: 213–234.

Vacher, L. G., Piani, L., Rigaudier, T., Thomassin, D., Florin, G., Piralla, M., and Marrocchi, Y. 2020. Hydrogen in Chondrites: Influence of Parent Body Alteration and Atmospheric Contamination on Primordial Components. *Geochimica et Cosmochimica Acta* 281: 53–66.

Vacher, L. G., Piralla, M., Gounelle, M., Bizzarro, M., and Marrocchi, Y. 2019. Thermal Evolution of Hydrated Asteroids Inferred from Oxygen Isotopes. *The Astrophysical Journal Letters* 882: L20.

Velbel, M. A. 2014. Stoichiometric Reactions Describing Serpentinization of Anhydrous Primary Silicates: A Critical Appraisal, with Application to Aqueous Alteration of Chondrule Silicates in CM Carbonaceous Chondrites. *Clays and Clay Minerals* 62: 126–136.

Velbel, M. A., Tonui, E. K., and Zolensky, M. E. 2012. Replacement of Olivine by Serpentine in the Carbonaceous

Chondrite Nogoya (CM2). *Geochimica et Cosmochimica Acta* 87: 117–135.

Velbel, M. A., Tonui, E. K., and Zolensky, M. E. 2015. Replacement of Olivine by Serpentine in the Queen Alexandra Range 93005 Carbonaceous Chondrite (CM2): Reactant–Product Compositional Relations, and Isovolumetric Constraints on Reaction Stoichiometry and Elemental Mobility during Aqueous Alteration. *Geochimica et Cosmochimica Acta* 148: 402–425.

Verdier-Paoletti, M. J., Marrocchi, Y., Vacher, L. G., Gattacceca, J., Gurenko, A., Sonzogni, C., and Gounelle, M. 2019. Testing the Genetic Relationship between Fluid Alteration and Brecciation in CM Chondrites. *Meteoritics & Planetary Science* 54: 1692–1709.

Villalon, K., Ohtaki, K., Bradley, J., Ishii, H., Davis, A., and Stephan, T. 2021. Search for Meteoritic GEMS II: Comparison of Inclusions in Amorphous Silicates from the Paris Chondrite and from Anhydrous Chondritic Interplanetary Dust Particles. *Geochimica et Cosmochimica Acta* 310: 346–362.

Weisberg, M. K., McCoy, T. J., and Krot, A. N. 2006. Systematics and Evaluation of Meteorite Classification. *Meteorites and the Early Solar System II* 19: 19–52.

Wogelius, R. A., and Walther, J. V. 1992. Olivine Dissolution Kinetics at Near-Surface Conditions. *Chemical Geology* 97: 101–112.

Yang, X., Hanna, R. D., Davis, A. M., Neander, A. I., and Heck, P. R. 2022. A Record of Post-Accretion Asteroid Surface Mixing Preserved in the Aguas Zarcas Meteorite. *Nature Astronomy* 6: 1051–58.

Zanetta, P.-M., Le Guillou, C., Leroux, H., Zanda, B., Hewins, R., and Bellino, G. 2022. Processes and Temperatures of FGR Formation in Chondrites. *Geochimica et Cosmochimica Acta* 319: 94–117.

Zanetta, P.-M., Leroux, H., Le Guillou, C., Zanda, B., and Hewins, R. 2021. Nebular Thermal Processing of Accretionary Fine-Grained Rims in the Paris CM Chondrite. *Geochimica et Cosmochimica Acta* 295: 135–154.

Zhang, L. 2013. Aspects of Rock Permeability. *Frontiers of Structural and Civil Engineering* 7: 102–116.

Zolensky, M. E., Barrett, R., and Browning, L. 1993. Mineralogy and Composition of Matrix and Chondrule Rims in Carbonaceous Chondrites. *Geochimica et Cosmochimica Acta* 57: 3123–48.

Zolensky, M. E., Mittlefehldt, D. W., Lipschutz, M. E., Wang, M.-S., Clayton, R. N., Mayeda, T. K., Grady, M. M., Pillinger, C., and David, B. 1997. CM Chondrites Exhibit the Complete Petrologic Range from Type 2 to 1. *Geochimica et Cosmochimica Acta* 61: 5099–5115.

## SUPPORTING INFORMATION

Additional supporting information may be found in the online version of this article.

**Figure S1.** EDS maps of Winchcombe meteorite sections. (a–f) Lithology A. Mg (red), Fe (green), and Ca (blue) highlight olivine in bright red and phyllosilicates in dark, and carbonates in blue and TCI-like objects in green.

**Figure S2.** EDS maps of Winchcombe meteorite sections. (a) Lithology B, (b–d) lithology B and Mx; (e) lithology B, H, and Mx. Mg (red), Fe (green), and Ca (blue) highlight olivine in bright red and phyllosilicates in dark, and carbonates in blue and TCI-like objects in green.

**Figure S3.** EDS maps of Winchcombe meteorite sections. (a) Lithology C; (b) lithology D and Mx; (c) lithology E; (d) lithology H, G, and B; (e) lithology Mx. Mg (red), Fe (green), and Ca (blue) highlight olivine in bright red and phyllosilicates in dark, and carbonates in blue and TCI-like objects in green.

**Figure S4.** Ternary plots (atom%) of the WDS-EPMA and EDS measurements of the fine-grained and secondary components present within Winchcombe lithologies. From top to bottom, the components measured are FGRs, matrix, rims to TCI-like objects, cores to TCI-like objects, and other phyllosilicates found within chondrules, calcium-aluminum-rich inclusions, etc. From left to right, ternary diagrams show the variation between Fe versus Mg versus S, Fe versus Mg versus Al+Si and Fe+Mg versus S versus Al+Si, respectively. Colors are used to distinguish EDS and WDS-EPMA measurements from different lithologies.

**Figure S5.** Graphs of the WDS-EPMA and EDS measurements of the fine-grained and secondary components present within Winchcombe lithologies. From top to bottom, the components measured are FGRs, matrix, rims to TCI-like objects, cores to TCI-like objects, and other phyllosilicates found within chondrules and calcium-aluminum-rich inclusions. From left to right, graphs show Si/Al versus Mg#, (Si+Al)/(Si+Al+Mg+Fe) versus Mg#, and S versus Mg# (all atom%). Colors are used to distinguish EDS and WDS-EPMA measurements from different lithologies within Winchcombe.

**Figure S6.** BSE images of carbonate grains in P30540 (lithology F). (a) A grain of dolomite (D) that contains an irregular patch of Ca-carbonate (arrowed) and is adjacent to a larger polycrystalline grain of Ca-carbonate (Cc). (b) A polymineralic grain comprising patches of Ca-carbonate (Cc) that are rimmed by Fe-rich phyllosilicate (white) and dolomite (D). (c) The area outlined by the dashed white lines in (B) showing euhedral dolomite associated with phyllosilicate (white) and Ca-carbonate (Cc). Grains of Ca-carbonate in P30552 [lithology A]. (d, f) Are SE images, and (e, g) SEM-CL. (d, e) Show a TCI-like object rimmed calcite (Cal) grain with areas of different CL intensity, the boundaries between some of which line up with fractures visible in the BSE image. The Cal grain in (f) and (Gd) is featureless in BSE but contains rectilinear areas differing in CL intensity.

**Table S1.** Summary of 3-D petrofabric analysis by μCT of Winchcombe fragments.

**Table S2.** Fluid flow modeling results of the permeability in the $xyz$ direction of each of the four sub volumes from μCT data from BM.2022,M2,34.

**File S1.** Images and stereographic projection of all 3-D petrofabric analysis of the Winchcombe μCT data.

**Data S1.** Brecciation at the grain scale within the lithologies of the Winchcombe CM carbonaceous chondrite.

**Excel Spreadsheet 2–6.** Combined WDS-EPMA and EDS quantitative chemical analysis for major and minor element abundances. Each spreadsheet is related to measurements from a particular component: (1) FGR, (2) Matrix, (3) TCI-like object-rims, (4) TCI-like object-cores, (5) Phyllosilicates in chondrules, calcium-aluminum-rich inclusions, etc. Data are presented as both wt% and normalized atom%.